TUNABLE ELASTOMERIC NANO-CHANNELS FROM GUIDED FRACTURE FOR BIOPOLYMER SUPER RESOLUTION IMAGING

A Dissertation
Presented to
The Academic Faculty

by

Han-Ching Chiu

In Partial Fulfillment
of the Requirements for the Degree
Doctor of Philosophy in the
Department of Biomedical Engineering

Georgia Institute of Technology & Emory University
December 2019

TUNABLE ELASTOMERIC NANO-CHANNELS FROM GUIDED FRACTURE FOR BIOPOLYMER SUPER-RESOLUTION IMAGING

Approved by:

Dr. Shuichi Takayama, Advisor
School of Biomedical Engineering
Georgia Institute of Technology

Dr. Michael Thouless
School of Mechanical Engineering
University of Michigan

Dr. Philip Santangelo
School of Biomedical Engineering
Georgia Institute of Technology

Dr. Yifan Liu
Department of Pathology
University of Michigan

Dr. Todd Sulchek
School of Mechanical Engineering
Georgia Institute of Technology

Date Approved: October 21, 2019

To friends and family

ACKNOWLEDGEMENTS

First and foremost, I would like to thank my advisor Shuichi Takayama. I feel extremely fortunate to be mentored by such a great educator, not just in research, but also in the way of life. Professor Takayama truly stands out as an all-around advisor. When research is progressing well, he exemplifies the excitements that one would envision a researcher to be. When results aren't ideal, somehow Professor Takayama is always able to find the useful, salvageable parts. In life, Professor Takayama exudes calmness and warmth that reassures his students that he will always have our backs. Suffice to say that without his guidance, I would not be able to go through the process of graduate studies.

I would also like to thank Professor Michael Thouless and Yifan Liu. Both of whom are constant presence that guided me through this thesis. I am also grateful to them for their participations at my defense and their continual supports and collaborations after Takayama Lab's relocation from University of Michigan to Georgia Tech. I would also like to thank my committee members Professor Santangelo and Sulchek for their constructive criticism and comments.

My sincere thanks and appreciations to Nick Ginga and Ji-Hoon Lee, my comrades in the nanochannel project. The stretcher project would not have gone far without their hard work and input. Especially to Nick who reminded me continuously to pivot, pivot, and pivot whenever the project hit a wall. I would also like to express my gratitude towards Byoung Choul Kim, who laid the groundwork for this project and trained me on hands-on skillsets. I would also like to recognize the collaboration with Izzy Newton from Prof. Thouless lab who also worked on the project.

I am incredibly lucky to be in the Takayama Lab, a supportive and friendly group. Over the years that I've worked alongside gifted colleagues, Cameron Yamanishi, Ge-Ah Kim, David Mertz, Stephen Robinson, Midori Maeda and Tasdiq Ahmed, Yang Song, Xinyu Lu, Taisuke Kojima a merry crew of graduate students and post-docs that came to Georgia Tech together from Umich and the GaTech members like Eric Parigoris, Johnathan Chang, Hannah Viola, Katherine Nguyen and Vishwa Vasani, not to mention the troops of visiting scholars and students who passed by the lab, Tina Yang, Hao-Chen Chang, Yoshinobu Murayama and many, many more. Thank you all for the years of encouragements, assistance and laughter.

I would also like to thank the people who supported me along the way outside of school. My friends, Mia Li, Chun-Wen Chen, and William Chu, Xsiao-Ting Huang, Hien Pham for your companionship and listening to me complained about nothing and everything. Last but not least, my family for their unending support over the years, my mother and my father for their love and belief in me, and my sister, who pushed me like no other.

TABLE OF CONTENTS

LIST OF TABLES

LIST OF FIGURES

LIST OF SYMBOLS AND ABBREVIATIONS

Δ	delta, indicating differences between two numbers
°	Degree (angle)
°C	degrees Celsius, a temperature unit
a.u.	Arbitrary units
AFM	Atomic force microscopy
AU	Active units
BME	2-Mercaptoethanol
BrdU	Bromodeoxyuridine / 5-bromo-2'-deoxyuridine
CAD	computer-aided design
Cd^{2+}	Cadmium ion
$CdCl_2$	Cadmium chloride
ChIP	Chromatin immunoprecipitation
CLiC	Convex lens-induced confinement
DI	deionized
DNA	deoxyribonucleic acid
DNase	deoxyribonuclease
dSTORM	direct stochastic optical reconstruction microscopy
EDTA	Ethylenediaminetetraacetic acid
EdU	5-ethynyl-2'-deoxyuridine
E_f	Young's modulus of thin film
FISH	Fluorescence in situ hybridization
fL	Femtoliter, a volume unit

g	Gram, a mass unit
Gloxy	glucose oxidase and Catalase
GUI	Graphical user interface
H	Histone protein
h	Thickness of thin film
H_2O	water
HA	Hemagluttanin protein
HP1	heterochromatin protein 1
h-PDMS	Hard polydimethylsiloxane
hr	Hour, a time unit
i.e.	id est, meaning in other words
K	lysine
kb	kilo-basepairs
L	Liter, a volume unit
M	Molar concentration
mbar	millibar, a pressure unit
me	Methyl group
MEA	Cysteamine
$MgCl_2$	Magnesium chloride
min	minutes
mKO	mKusabira Orange fluorescent protein
MLA	Maskless aligner
mm	Millimeter, a length unit
mM	Millimolar, a concentration unit
MTT	metallothionein gene

N	Newton, a force unit
NaCl	Sodium chloride
nm	Nanometer, a length unit
OxEA	OxyErase solution
PBS	Phosphate buffer saline
PDMS	polydimethylsiloxane
pg	Picogram, a mass unit
pH	negative logarithm of hydrogen ion concentration
PMSF	phenylmethanesulfonyl fluoride
RNase	ribonucleases
rpm	Revolutions per minute, a rotation speed unit
sec, s^{-1}	Second, a time unit
SEM	Scanning electron microscopy
SPP	Culture medium for *Tetrahymena*
TEM	Tunneling electron microscopy
Tris-HCl	Tris hydrochloride
UV	Ultra-violet
W	Watt, a power unit
w/v	mass/volume percent
w/w	Weight percentage
x	times, multiplication factor
xg	Gravity of centrifuge
YOYO	Oxazole Yellow, a DNA intercalating dye
Γ_f	Toughness of thin film
ε_0	Critical strain

λ-DNA	Lambda phage deoxyribonucleic acid
μL	Microliter, a unit for volume
μm	Micrometer, a unit for length
μM	Micromolar, a unit for concentration

SUMMARY

This thesis describes the development of a polydimethylsiloxane (PDMS) based micro-, nano-fluidics system compatible with super-resolution imaging to capture and linearize extracted chromatin, for epigenetics studies. Native chromatin are DNA folded and tightly coiled around proteins, to access the proteins of interest, chromatin must be unwrapped via linearization. An array of cracks ranging from micron-scale to nano-scale is fabricated by subjecting a two-layer elastomeric materials system to an applied tensile strain. The morphology of the generated surface cracks is determined by the pre-patterned photoresist features in a PDMS substrate and the spin coated thin film on its surface. The depths of the cracks are governed by the thickness and properties of the spin-coated surface layer, while the locations of crack initiation are determined by pre-patterned features in the bulk substrate. The surface cracks are sealed with a thin PDMS film by plasma bonding. This creates channels from the surface cracks, where the channel widths can be tuned via an automated stretcher that applies a uniaxial strain. This tunable device can be used to capture biopolymers such as DNA and chromatin. The linearization of captured biopolymers is achieved by a combination of nano-confinement in small conduits and the squeezing hydrodynamic flow which results from the strain being released from the stretcher. Various fluorescent dyes are investigated to overcome the oxygen rich PDMS environment that is not conducive to super-resolution microscopy. *Tetrahymena thermophila*, a protozoan, is chosen as the model system for chromatin extraction and the protein of interest is labeled with super-resolution compatible dye. Thus, direct super resolution imaging of proteins on biopolymers in the tunable nano-channels is achieved.

Visualization of the linearized chromatin pointed towards dispersive segregation for histone deposition. We believe that this linearization platform can be adapted for visualization of other protein modifications and eventually provide valuable epigenetic information.

CHAPTER 1. INTRODUCTION

1.1 What is epigenetics

Epigenetics is the study of how epigenetic marks tell genes to behave. Changes in the epigenome can be affected by external influences without disturbing the underlying DNA sequences. Many of these epigenetic marks are associated with, but not limited to, DNA methylation or proteins modifications on the DNA structure. Therefore, to maintain genome stability, not only is the conservation of DNA sequence crucial, the preservation of chromatin structure is also of great importance. Disruption of chromatin structure could lead to changes in cell fate determination, gene expression, tissue regeneration, potential cell deaths, cancer and other diseases (John and Rougeulle, 2018; Kanherkar et al., 2014; Morales et al., 2001).

In order to pack DNA into the nucleus of a cell, it is necessary to condense the biopolymers into a small, compact, rod like structure – chromatin. DNA wraps around a histone octamer core made up of two dimers (H2A/H2B) and one tetramer $(H3/H4)_2$ through electrostatic interactions, Figure 1.1A. These histones provide sites for protein modifications that subsequently affect chromatin structure and accessibility of DNA sequences (Gates et al., 2017; Kornberg, 1974). During DNA replication, chromatin structures are disrupted, the nucleosomes unwrapped, and the histone cores disassembled to accommodate replication forks and other replication machineries. New histones are synthesized and eventually incorporated into chromatin. One key challenge in studying the inheritance of epigenetic marks on chromatin lie in the understanding of the mechanisms and kinetics of how epigenetic marks are restored onto the newly synthesized chromatin

(Annunziato, 2012; Henikoff et al., 2004; McKittrick et al., 2004; Workman and Abmayr, 2004).

It is unclear whether the transmissions of old and newly synthesized histone followes a dispersive or conservative manner, Figure 1.1B. The conservative segregation transmission theory postulates that old histones are distributed preferentially onto one arm of the replication fork, favoring either the leading strand or the lagging strand, while the dispersive segregation argues for random distribution to both strands. Contradictory results for either hypothesis exist (Cusick et al., 1984; Jackson, 1988; Krude and Knippers, 1991; Seale, 1976; Seidman et al., 1979; Weintraub, 1976). It is hypothesized that information for gene activity control is carried within chromatin as various DNA-protein structures, and that the heterogeneity of such DNA packaging would result in an inactive or active transcriptional state.

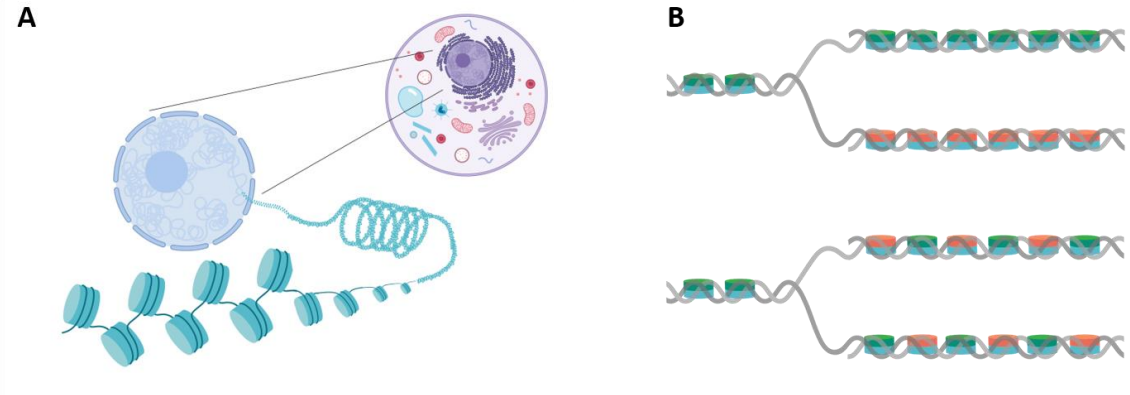

Figure 1.1 Chromatin structure and histone distribution models. (A) Molecular biology view of beads-on-a-string structure of chromatin. (B) Top: conservative segregation model, Bottom: dispersive segregation model.

1.2 Methods for chromatin studies – Non linearization method

Chromatin immunoprecipitation (ChIP) is the most widely used analysis tool for studying chromatin for decades now (Lippman et al., 2003). The key elements of this technique involved crosslinking proteins to DNA or nuclease digestion, fragmentation of DNA-protein complexes, immunoprecipitation of DNA-protein complexes with antibodies followed by purification for subsequent analysis, Figure 1.2. The availability, affinity and specificity of the antibodies therefore play a key role in discriminating between protein variants and its associated modifications. Traditionally this method is limited by the need for large sample quantities and its ability to perform multiple histone modification detections. Advances in microfluidics in recent years have improved the throughput and enabled automation. The technique is also expanded into genome scale analysis with the use of ChIP-chip microarrays and ChIP-seq technology (Adli and Bernstein, 2011; Egan et al., 2016; Lee et al., 2015).

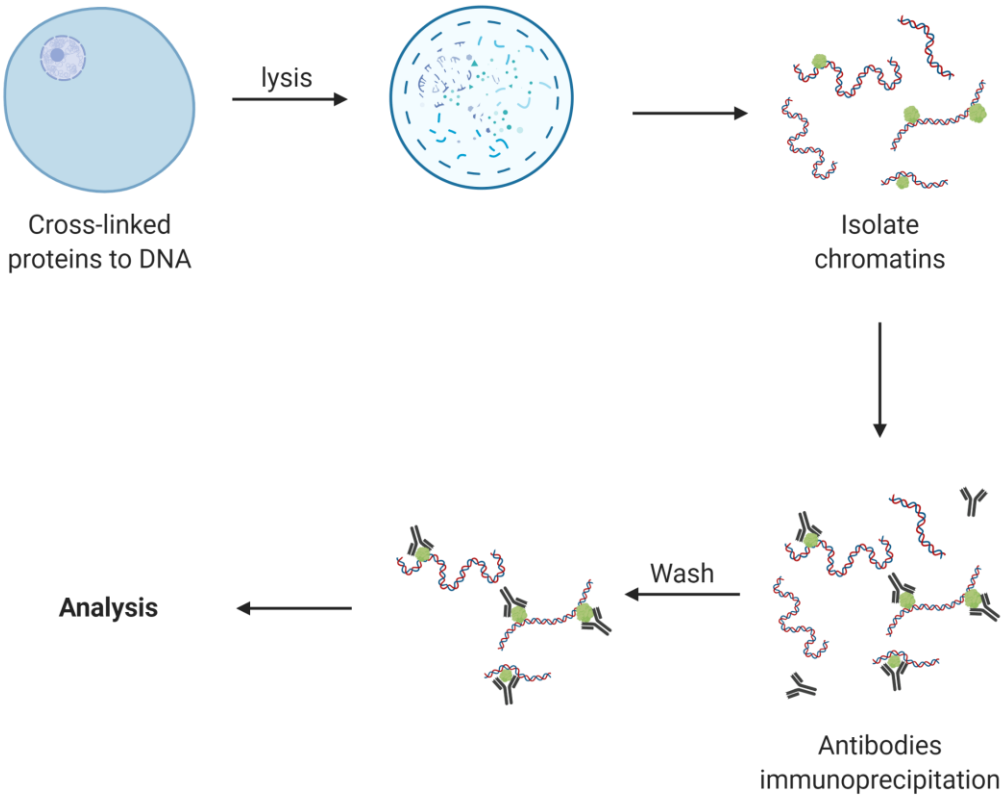

Figure 1.2 Chromatin Immunoprecipitation procedure. Proteins are crosslinked to the DNA backbone in vivo Chromatin are isolated and fragmented. Antibodies are used to immunoprecipitated out the target protein/DNA complex, followed by reverse crosslinking and digestion of proteins for further analysis.

ChIP has been used to detect nucleosome positioning. For instance, Haberle et al., 2014, mapped the precise positioning patterns of H3K4me3 and showed that it is independent of TATA-box-binding protein recruitment. ChIP-chip has also been used in histone modification analysis to profile five histone modifications, H3, acetylated H4, acetylated H3, monomethylated H3K4 and demethylated H3K4 to look at histone

modifications promoter activities and its implications on transcriptional regulatory activities (Heintzman et al., 2007).

Novel ChIP assays combing microfluidics have been presented as solutions to overcome restrictions on traditional assays, such as long assay time, large sample size requirement. Teste et al., 2017, combined a microfluidic droplet assay which reduces cell number requirement to tens of thousands compared to the hundreds of thousands to millions of cells required and decrease assay time by increasing reaction kinetics, while the magnetic beads and tweezers combination facilitates transport of DNA between the antibodies binding, extraction and washing steps necessary in a ChIP assay. Recently, microfluidic based droplet assays using ChIP enriched samples were presented as ChIA-Drop which boasted an even lower sample size requirement (Zheng et al., 2019). An even lower number of sample size can be achieved using a semi-automated microfluidic system. This microfluidic device utilized sieve valves to enrich chromatin and perform wash steps with only 2000 cells required (Wu et al., 2009).

Despite the advancement in combining microfluidics with ChIP assays, innovations in chromatin assays are still required for various unmet needs, such as the ability to assay single cells or single molecules, the inherent difficulties to assay proteins that are indirectly associated with DNA (Wardle and Tan, 2015). Long read sequence information also tends to be lost due to fragmentations. If the chromatin were prepared by crosslinking proteins and DNA, there may be potential implications on arresting functional interactions; while selective digestion is a possibility with the nuclease methods. The quality control of antibody specificity and affinity is also of great importance for interpreting ChIP data.

Furthermore, the ability to detect multiple modifications in one assay would be advantageous and remained a challenge at present (Park, 2009; Truch et al., 2018).

1.3 Methods for chromatin studies – Linearization method

In contrast to the ChIP methodology where chromatin disentangling was achieved by mechanical shearing of the biopolymers into tiny fragments, thus potentially losing epigenetic information, an alternative method for studying chromatin and histone modifications is by the use of linearization of chromatin followed by image analysis such as atomic force microscopy, electron microscopy, and optical microscopy. Common methods for chromatin linearization involved either molecular combing to uniformly stretch arrays of DNA or chromatin by meniscus retraction; the use of end-tethered stretching; direct cell shearing; or nanochannels which utilized the self-avoidance interactions of bio-polymers in confinement below its persistence length to induce chromatin untangling.

1.3.1 Combing

A micro-droplet of extracted chromatin is placed atop of a PDMS stamp containing arrays of microstructures in the shape of shallow wells. The meniscus of chromatin was dragged across the surface of the PDMS stamp at a controlled speed (Cerf et al., 2012). The dragging motion combined with the meniscus evaporation would stretch out chromatin fibers. Transfer to glass coverslips for further analysis can be achieved by simple stamping. This method does not require tethers to trap and position chromatin fibers, Figure 1.3. The resulting linearized chromatin is investigated with AFM showing nucleosome distribution. This approach can also be combined with fluorescent microscopy, labelling histones with

fluorophore tagged antibodies. Despite the high throughput-ness of this technique, biopolymer stretching is determined by the retraction length, therefore limiting the sample range.

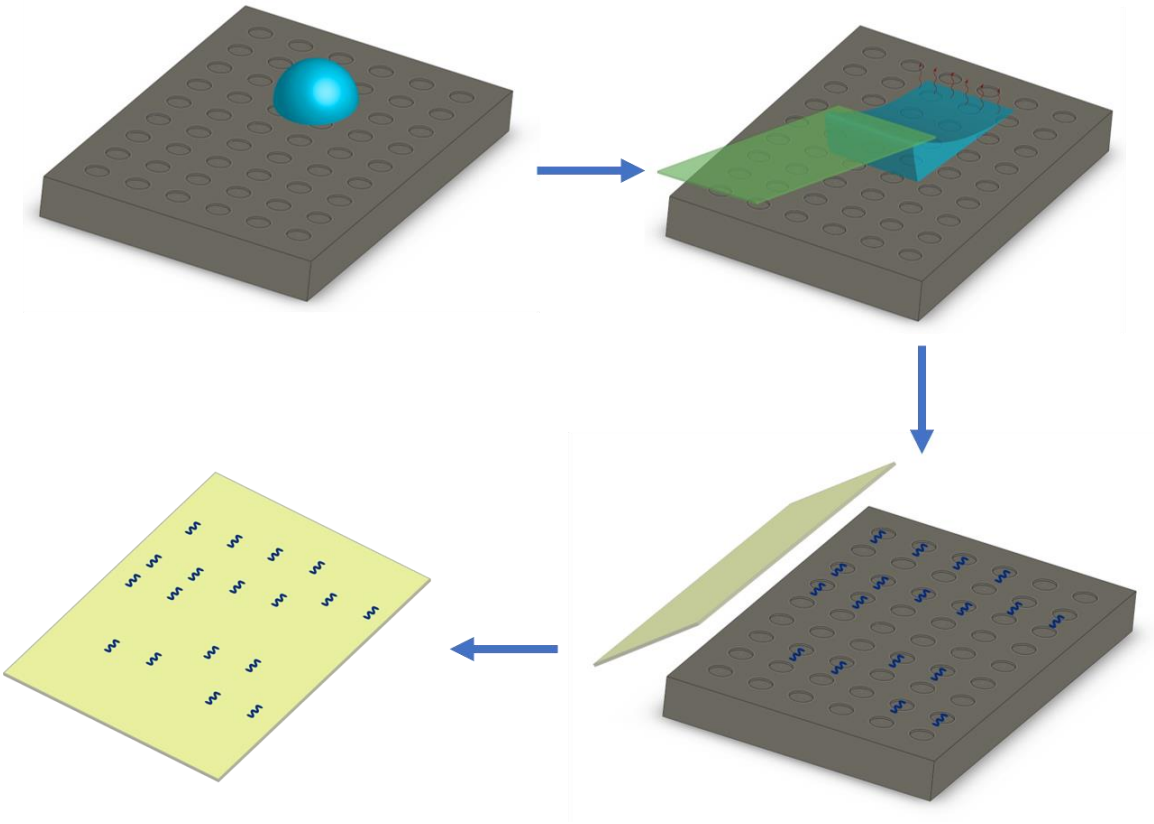

Figure 1.3 Chromatin combing procedure. Droplet is deposited on PDMS stamp. Meniscus is dragged across the surface at fixed speed. The shearing of the dragging motion combined with evaporation of the solution leaving the elongated chromatin on the PDMS surface. Stamping of the PDMS will transfer the stretched chromatin to the glass slide.

1.3.2 End-tethering stretching

End-tethering stretching of chromatin are often assisted by optical or magnetic tweezers (Bennink et al., 2001; Cui and Bustamante, 2000; Kaczmarczyk et al., 2018;

Leuba et al., 2003; Oana et al., 2014). For instance, Bennink et al. attached streptavidin conjugated beads to the ends of DNA molecules. The beads-tagged biopolymers are held to a micropipette tip through suction in a flow cell. Using optical tweezers, the chromatin is unraveled through force extension. Similarly, magnetic tweezers were used instead of optical tweezers by Leuba et al., 2003. One end of the biopolymer is tethered to a magnetic bead to the side of a cuvette and extension is achieved through a magnetic field, Figure 1.4. These tweezer-assisted type of extension methods are commonly used to investigate the mechanical properties and structure of chromatin fibers. However, the dimensional scale of interest for biomolecular questions such as histone modifications, nucleosome assembly requires techniques such as super-resolution microscopy or electron microscopy, that are not readily compatible with end-tethering techniques.

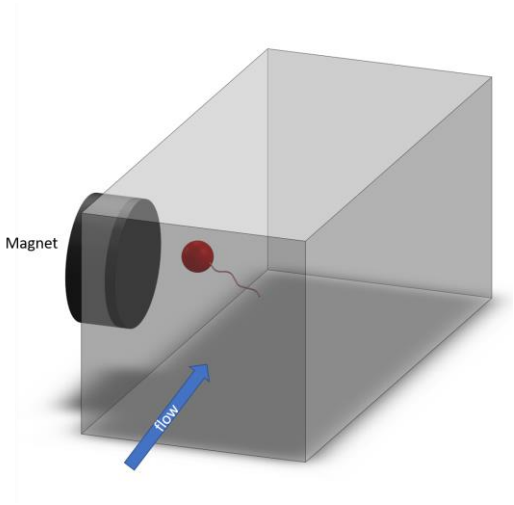

Figure 1.4 Magnetic tweezers for tethered chromatin elongation. Magnetic bead tagged DNA is suspended alongside a cuvette with a magnet.

1.3.3 Direct cell shearing

Direct cell shearing is another chromatin linearization technique that can be combined with Fluorescence *in situ* hybridization (FISH). Cells are subjected to alkaline treatment to release free chromatin and fixed onto a glass slide followed by fluorescent hybridization (Heng et al., 1992; Michalet et al., 1997; Senger et al., 1994). Chromatin extension in this method is not uniform. However, this technique provides opportunities to probe multiple modifications at once and can be utilized with super-resolution microscopy, Figure 1.5.

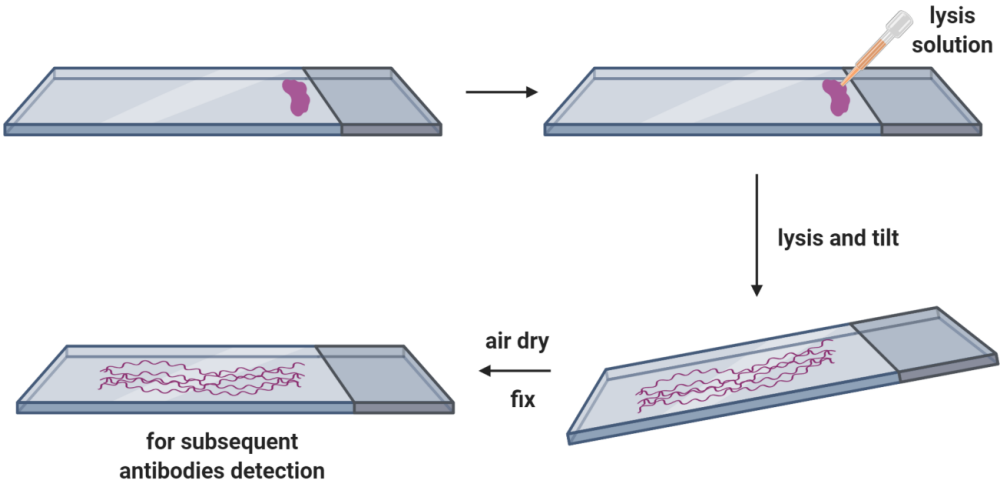

Figure 1.5 Direct cell lysis linearization procedure. Cells are directly deposited onto a glass slide. Lysis solution is deposited onto the droplet and incubated for cell lysis. The glass slid is tilted and chromatin or DNA are unfolded. The sample is left to air dry and followed by fixation and antibodies labeling of target proteins.

Wooten et al., 2018 adapted the direct cell lysis and fixation technique to linearize chromatin from *Drosophila* onto a glass slide. Newly synthesized DNA strands are labeled with EdU, while the chromatin fibers are stained with nucleoid intercalating dye YOYO-

3. Dual color histone labeling was achieved by green fluorescent protein on old H3 and H3.3 variant, while newly synthesized H3 and H3.3 were labeled with mKO. Paired with stimulated emission depletion microscopy, a super-resolution microscopy technique, chromatin extracted from *Drosophilia* germline stem cells showed asymmetry between old H3 and new H3, while conversely, old H3.3 variants do not exhibit asymmetric inheritance.

1.3.4 Confinement

Stretching via confinement in a nanochannel is another option for chromatin linearization (Benková et al., 2015). This method, however, is not as prevalent as the direct cell lysis methods, despite mapping DNA sequence with nanochannel has been practiced consistently (Basak et al., 2019; Levy and Craighead, 2010). Streng et al., 2009, demonstrated this method using reconstituted chromatin, comprised of λ-DNA and histone proteins. Nanochannels of this type are often prepared with fused silica through differential etching or electron beam lithography and chromatin linearization is achieved with an external electric field. Similarly, Yeh and Szeto, 2017, looked at chromatin extracted from HeLa cells with green fluorescent protein labeled H2B in silica nanoslits and the chromatin are furthered anchored by tethering one end to a microsphere. The removal of electric field in this method would relax chromatin fibers back into its compact and coiled state.

Convex Lens-induced Confinement (CLiC) is another linearization method utilizing nanostructure to achieve biopolymer extension (Berard et al., 2016; Henkin et al., 2016). Instead of an applied electric field to stretch out DNA, CLiC employed external forces to confine and linearize fibers. The nanogrooves on the CLiC flow cells are prepared by electron beam lithography on a coverslip, with another coverslip up top to seal off the

channel. DNA solution is loaded into the flow cell via capillary flow. As CLiC lens is slowly lowered and thusly pressure is applied to deform the top coverslip, nanogrooves acting as entropic traps will linearize DNA, Figure 1.6(B). Similar to the CLiC lens, a tunable channel with z-axis pressure driven narrowing is used to linearize DNA (Yu et al., 2018). A tri-layered structure controlled by pneumatic microvalve can push the interlayer polymer downwards to collapse the large microchannel, forming triangular shaped nanoslits for DNA stretching, Figure 1.6(C). However, neither methods have been applied to chromatin fiber extension. Furthermore, the use of an external force from the CLiC lens or the pressure driven flow in Yu et al., both limit the adaption of this method to commercial super-resolution microscopy, therefore constraining the types of data that can be extracted from such techniques.

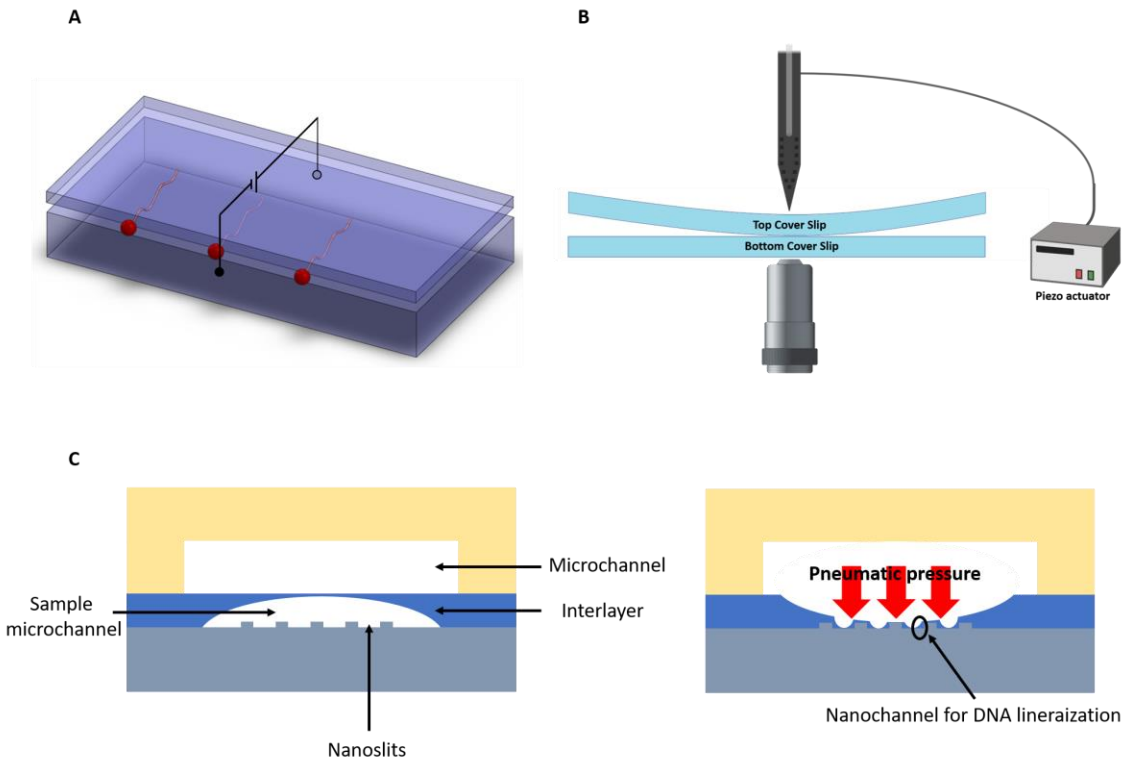

Figure 1.6 Nano-confinement methods for linearization. (A) End tethered chromatin in nanoslit with electric field assisted linearization. (B) CLiC scope using z-axis external force to deform top coverslip and linearize biopolymers in nanogrooves. (C) Pneumatic microvalves to collapse the interlayer in a trilayered device, forming triangular shapes nanochannel for DNA linearizations.

1.4 Perspectives

Great strides have been made in the pursuit of epigenetic studies. The knowledge that we are able to glean from the biological systems, however, is only as good as the technologies available. Each of the techniques presented above has its advantages and disadvantages. There is no one system that would provide all the answer that is needed. The primary limitations faced by these techniques include the quantity of sample required; analysis from single cell is not yet available; the dependence on antibodies and optical

visualization thresholds implied the challenges in obtaining images at resolution required, and optical crosstalk from using multiple fluorophores. Most of these limitations would also present difficulties in downstream signal processing. Furthermore, despite the promise of epigenetic therapy, at the time of writing, to implement epigenetic analysis into clinical setting is still a universal challenge for every technique. It would take efforts from multiple disciplines to engineer novel systems in the quest of elucidating the mechanism and kinetics involved in epigenome and eventually translate into medical practices. In this dissertation, expanding on the tunable fluidic system (Kim et al., 2014; Matsuoka et al., 2012), a strain induced fracture nanofluidic system is combined with super-resolution imaging technique to look at the inheritance of histones during DNA replication.

1.5 References

Adli, M., and Bernstein, B.E. (2011). Whole-genome chromatin profiling from limited numbers of cells using nano-ChIP-seq. Nat. Protoc. *6*, 1656–1668.

Annunziato, A.T. (2012). Assembling chromatin: The long and winding road. Biochim. Biophys. Acta - Gene Regul. Mech. *1819*, 196–210.

Basak, R., Liu, F., Qureshi, S., Gupta, N., Zhang, C., de Vries, R., van Kan, J.A., Dheen, S.T., and van der Maarel, J.R.C. (2019). Linearization and Labeling of Single-Stranded DNA for Optical Sequence Analysis. J. Phys. Chem. Lett. *10*, 316–321.

Benková, Z., Námer, P., and Cifra, P. (2015). Stripe to slab confinement for the linearization of macromolecules in nanochannels. Soft Matter *11*, 2279–2289.

Bennink, M.L., Leuba, S.H., Leno, G.H., Zlatanova, J., de Grooth, B.G., and Greve, J. (2001). Unfolding individual nucleosomes by stretching single chromatin fibers with optical tweezers. Nat. Struct. Biol. *8*, 606–610.

Berard, D.J., Shayegan, M., Michaud, F., Henkin, G., Scott, S., and Leslie, S. (2016). Formatting and ligating biopolymers using adjustable nanoconfinement. Appl. Phys. Lett. *109*, 033702.

Cerf, A., Tian, H.C., and Craighead, H.G. (2012). Ordered Arrays of Native Chromatin Molecules for High-Resolution Imaging and Analysis.

Cui, Y., and Bustamante, C. (2000). Pulling a single chromatin fiber reveals the forces that maintain its higher-order structure. Proc. Natl. Acad. Sci. U. S. A. *97*, 127–132.

Cusick, M.E., DePamphilis, M.L., and Wassarman, P.M. (1984). Dispersive segregation of nucleosomes during replication of simian virus 40 chromosomes. J. Mol. Biol. *178*, 249–271.

Egan, B., Yuan, C.-C., Craske, M.L., Labhart, P., Guler, G.D., Arnott, D., Maile, T.M., Busby, J., Henry, C., Kelly, T.K., et al. (2016). An Alternative Approach to ChIP-Seq Normalization Enables Detection of Genome-Wide Changes in Histone H3 Lysine 27 Trimethylation upon EZH2 Inhibition. PLoS One *11*, e0166438.

Gates, L.A., Foulds, C.E., and O'Malley, B.W. (2017). Histone Marks in the 'Driver's Seat': Functional Roles in Steering the Transcription Cycle. Trends Biochem. Sci. *42*, 977–989.

Haberle, V., Li, N., Hadzhiev, Y., Plessy, C., Previti, C., Nepal, C., Gehrig, J., Dong, X., Akalin, A., Suzuki, A.M., et al. (2014). Two independent transcription initiation codes overlap on vertebrate core promoters. Nature *507*, 381–385.

Heintzman, N.D., Stuart, R.K., Hon, G., Fu, Y., Ching, C.W., Hawkins, R.D., Barrera, L.O., Van Calcar, S., Qu, C., Ching, K.A., et al. (2007). Distinct and predictive chromatin signatures of transcriptional promoters and enhancers in the human genome. Nat. Genet. *39*, 311–318.

Heng, H.H., Squire, J., and Tsui, L.C. (1992). High-resolution mapping of mammalian genes by in situ hybridization to free chromatin. Proc. Natl. Acad. Sci. U. S. A. *89*, 9509–9513.

Henikoff, S., Furuyama, T., and Ahmad, K. (2004). Histone variants, nucleosome assembly and epigenetic inheritance. Trends Genet. *20*, 320–326.

Henkin, G., Berard, D., Stabile, F., Shayegan, M., Leith, J.S., and Leslie, S.R. (2016). Manipulating and Visualizing Molecular Interactions in Customized Nanoscale Spaces. Anal. Chem. *88*, 11100–11107.

Jackson, V. (1988). Deposition of newly synthesized histones: hybrid nucleosomes are not tandemly arranged on daughter DNA strands. Biochemistry *27*, 2109–2120.

John, R.M., and Rougeulle, C. (2018). Developmental Epigenetics: Phenotype and the Flexible Epigenome. Front. Cell Dev. Biol. *6*, 130.

Kaczmarczyk, A., Brouwer, T.B., Pham, C., Dekker, N.H., and van Noort, J. (2018). Probing Chromatin Structure with Magnetic Tweezers. (Humana Press, New York, NY), pp. 297–323.

Kanherkar, R.R., Bhatia-Dey, N., and Csoka, A.B. (2014). Epigenetics across the human lifespan. Front. Cell Dev. Biol. *2*, 49.

Kim, B.C., Moraes, C., Huang, J., Thouless, M.D., Takayama, S., Xia, X. -h., Koide, K., Thouless, M., Takayama, S., and Takayama, S. (2014). Fracture-based micro- and nanofabrication for biological applications. Biomater. Sci. *2*, 288.

Kornberg, R.D. (1974). Chromatin structure: A repeating unit of histones and DNA. Science (80-.). *184*, 868–871.

Krude, T., and Knippers, R. (1991). Transfer of nucleosomes from parental to replicated chromatin. Mol. Cell. Biol. *11*, 6257.

Lee, H.J., Lowdon, R.F., Maricque, B., Zhang, B., Stevens, M., Li, D., Johnson, S.L., and Wang, T. (2015). Developmental enhancers revealed by extensive DNA methylome maps of zebrafish early embryos. Nat. Commun. *6*, 6315.

Leuba, S.H., Karymov, M.A., Tomschik, M., Ramjit, R., Smith, P., and Zlatanova, J. (2003). Assembly of single chromatin fibers depends on the tension in the DNA molecule: Magnetic tweezers study. Proc. Natl. Acad. Sci. U. S. A. *100*, 495–500.

Levy, S.L., and Craighead, H.G. (2010). DNA manipulation, sorting, and mapping in nanofluidic systems. Chem. Soc. Rev. *39*, 1133.

Lippman, Z., May, B., Yordan, C., Singer, T., and Martienssen, R. (2003). Distinct Mechanisms Determine Transposon Inheritance and Methylation via Small Interfering RNA and Histone Modification. PLoS Biol. *1*, e67.

Matsuoka, T., Kim, B.C., Huang, J., Douville, N.J., Thouless, M.D., and Takayama, S. (2012). Nanoscale squeezing in elastomeric nanochannels for single chromatin linearization. Nano Lett. *12*, 6480–6484.

McKittrick, E., Gafken, P.R., Ahmad, K., and Henikoff, S. (2004). From The Cover: Histone H3.3 is enriched in covalent modifications associated with active chromatin. Proc. Natl. Acad. Sci. *101*, 1525–1530.

Michalet, X., Ekong, R., Fougerousse, F., Rousseaux, S., Schurra, C., Hornigold, N., Van Slegtenhorst, M., Wolfe, J., Povey, S., Beckmann, J.S., et al. (1997). Dynamic molecular combing: Stretching the whole human genome for high- resolution studies. Science (80-.). *277*, 1518–1523.

Morales, V., Giamarchi, C., Chailleux, C., Moro, F., Marsaud, V., Le Ricousse, S., and Richard-Foy, H. (2001). Chromatin structure and dynamics: Functional implications. Biochimie *83*, 1029–1039.

Oana, H., Nishikawa, K., Matsuhara, H., Yamamoto, A., Yamamoto, T.G., Haraguchi, T., Hiraoka, Y., and Washizu, M. (2014). Non-destructive handling of individual chromatin fibers isolated from single cells in a microfluidic device utilizing an optically driven microtool. Lab Chip *14*, 696–704.

Park, P.J. (2009). ChIP-seq: advantages and challenges of a maturing technology. Nat. Rev.

Genet. *10*, 669–680.

Seale, R.L. (1976). Studies on the mode of segregation of histone nu bodies during replication in HeLa cells. Cell *9*, 423–429.

Seidman, M.M., Levine, A.J., and Weintraub, H. (1979). The asymmetric segregation of parental nucleosomes during chrosome replication. Cell *18*, 439–449.

Senger, G., A.Jones, T., Fldlerová, H., Sanséau, P., Trowsdale, J., Duff, M., and Sheer, D. (1994). Released chromatin: linearized DNA for high resolution fluorescence *in situ* hybridization. Hum. Mol. Genet. *3*, 1275–1280.

Streng, D.E., Lim, S.F., Pan, J., Karpusenka, A., and Riehn, R. (2009). Stretching chromatin through confinement. Lab Chip *9*, 2772.

Teste, B., Champ, J., Londono-Vallejo, A., Descroix, S., Malaquin, L., Viovy, J.-L., Draskovic, I., and Mottet, G. (2017). Chromatin immunoprecipitation in microfluidic droplets: towards fast and cheap analyses. Lab Chip *17*, 530–537.

Truch, J., Telenius, J., Higgs, D.R., and Gibbons, R.J. (2018). How to Tackle Challenging ChIP-Seq, with Long-Range Cross-Linking, Using ATRX as an Example. (Humana Press, New York, NY), pp. 105–130.

Wardle, F.C., and Tan, H. (2015). A ChIP on the shoulder? Chromatin immunoprecipitation and validation strategies for ChIP antibodies. F1000Research *4*, 235.

Weintraub, H. (1976). Cooperative alignment of nu bodies during chromosome replication in the presence of cycloheximide. Cell *9*, 419–422.

Wooten, M., Nizami, Z., Yang, X., Snedeker, J., Ranjan, R., Kim, J.M., Urban, E., Tran, V., Buss, J., Gall, J., et al. (2018). Asymmetric histone incorporation during DNA replication in Drosophila male germline stem cells. SSRN Electron. J.

Workman, J.L., and Abmayr, S.M. (2004). Histone H3 variants and modifications on transcribed genes. Proc. Natl. Acad. Sci. *101*, 1429–1430.

Wu, A.R., Hiatt, J.B., Lu, R., Attema, J.L., Lobo, N.A., Weissman, I.L., Clarke, M.F., and Quake, S.R. (2009). Automated microfluidic chromatin immunoprecipitation from 2,000 cells. Lab Chip *9*, 1365.

Yeh, J.-W., and Szeto, K. (2017). Electrophoretic stretching and imaging of single native chromatin fibers in nanoslits. Biomicrofluidics *11*, 044108.

Yu, M., Hou, Y., Song, R., Xu, X., and Yao, S. (2018). Tunable Confinement for Bridging Single-Cell Manipulation and Single-Molecule DNA Linearization. Small *14*, 1800229.

Zheng, M., Tian, S.Z., Capurso, D., Kim, M., Maurya, R., Lee, B., Piecuch, E., Gong, L., Zhu, J.J., Li, Z., et al. (2019). Multiplex chromatin interactions with single-molecule

precision. Nature *566*, 558–562.

CHAPTER 2. FABRICATION OF TUNABLE NANOCHANNELS AND CONTROL OF UNIFORM CRACK ARRAYS IN ELASTOMERIC THIN FILM.

2.1 Abstract

Nanoscale channels with tunable width resulting from crack formations in a two-layer thin film system are presented here. In this study, we describe the generation of parallel nano-cracks by subjecting a nanoscale thin h-PDMS film/bulk PDMS system to an applied tensile strain. This material system is achieved by slow speed spin coating of h-PDMS to control the thin film thickness on a mold with predefined SU-8 photoresist features. We investigated the effect of SU-8 thickness and compositions on the topography of spin-coated h-PDMS films and the morphology of the cracks. The effect of the configuration of strain relieving notch pattern was explored and applied onto the system to achieve control of generation and propagation of cracks. This fabrication method allowed for these tunable nanochannels to be incorporated into a microfluidic system for DNA linearization. The capability of these channels to confine and linearize DNA are demonstrated with λ-DNA and 18.8 % of the molecules achieved nearly its expected tertiary structure length.

2.2 Introduction

Linearization of biopolymers with the use of nanochannels is a potential approach for future high-throughput technologies for genome mapping and epigenetic studies (De Carli et al., 2018; Douville et al., 2008; Lam et al., 2012; Riehn et al., 2005). However, the

fabrication of nanochannels is a non-trivial process using conventional e-beam lithography (Bilenberg et al., 2006; Mannion et al., 2006; Reccius et al., 2005) or nanoimprinting methods (Cho et al., 2010; L. Jay Guo et al., 2003). Furthermore, methods such as tapering channels, external electric field or the use of magnetic or optical tweezers to facilitate DNA loading are required for confinement and linearization of DNA. We previously demonstrated the use of multi-layered materials to generate periodic crack patterns in the oxidized surface layer of polydimethylsiloxane (PDMS) (Huh et al., 2007; Kim et al., 2014; Matsuoka et al., 2012; Mills et al., 2008, 2010; Zhu et al., 2005). This oxidized surface layer was created by subjecting bulk PDMS to an oxygen plasma. The approach of generating surface cracks in the oxidized layer of PDMS has fewer fabrication steps, but suffers from unreliable crack depths. The oxidized layer created is also highly dependent on the oxygen plasma system used, with the same plasma recipe not capable of being reproduced using different models of plasma oxidizer machines. Conversely, the h-PDMS thin film approach provides a more defined control of crack depth and reproducibility. The thickness of the h-PDMS layer is controlled by the spin coating process and consequently easier to be generalized.

The use of h-PDMS as the thin layer to generate micron scale cracks have been demonstrated previously (Kim et al., 2013, 2014). However, the continuation of this methodology to nanoscale thin films and cracks presents several challenges. In order for cracks to form in a thin film, fracture mechanics dictates that a level of critical strain must be reached (Huang et al., 2014; Mills et al., 2008). Below this critical strain, no cracks will form. Scaling a thin film's thickness from 11 μm to 200 nm increases the critical strain for fracture from ~ 21% to ~ 160% based on tabulated values using Equation (1) (Beuth, 1992).

To achieve the required elongation to reach the critical strain in the thin film, a mixture of PDMS with low Young's modulus is usually chosen as the substrate. However, at such a high strain, the bulk PDMS substrate often experiences catastrophic failure at the clamps of the stretching device before crack formation occurs in the thin film. It is therefore necessary to exchange the advantage of a high toughness PDMS mixture, high pre-polymer to crosslinker ratio, for the high strength of a low toughness PDMS mixture, low pre-polymer to crosslinker ratio, mixture so that the bulk PDMS would not break at the clamping regions. Another challenge to overcome with h-PDMS thin films is the generation of consistent parallel nanocracks. This is overcome by using a modified patterned saw-tooth SU-8 structure on h-PDMS mold as reported previously.

$$\epsilon_0 \sqrt{\frac{\overline{E_f} h}{\Gamma_f}} = 0.6 \tag{1}$$

2.3 Materials and methods

2.3.1 Device design and fabrication

Microchannels with v-notch strain relieving patterns were designed using AutoCAD, Figure 2.1(A). The SU-8 mold of this design was prepared with the Heidelberg Instruments MLA150 Maskless Aligner on silicon wafers using photolithography. Multiple thickness of 2 μm, 4 μm, 7 μm, and 20 μm of the SU-8 mold were prepared with SU-8 2, 2007, 2025 (Microchem) using the manufacturer's recommended recipes.

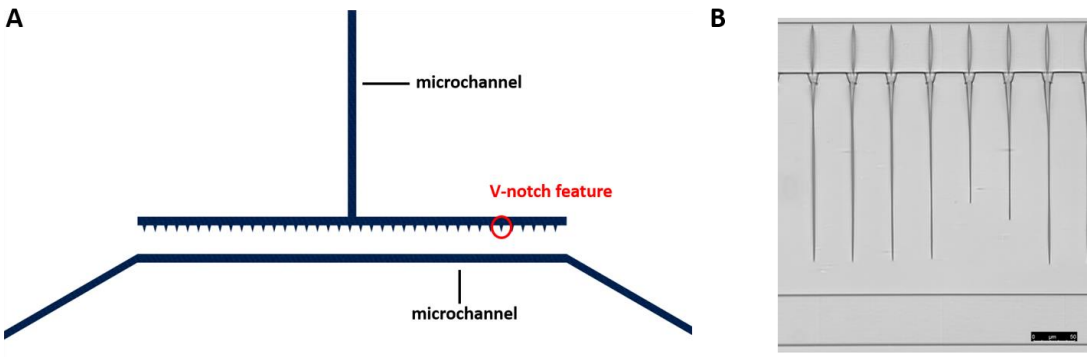

Figure 2.1 AutoCad device design. (A) Crack initiations are activated at the tip of the V-notch feature, eventually propagating through to connect the top and bottom microchannels with an applied tensile strain. (B) Optical image showing crack propagation from v-notches, scale bar = 50 μm.

The thin film h-PDMS layer was prepared using a modified protocol found in literature (Odom et al. 2002). The following reagents were added into a scintillation vial in sequence, 1.7 g of (7.0-8.0% vinylmethylsiloxane) – dimethylsiloxane copolymer, trimethylsiloxy terminated (VDT-731; Gelest Inc.), 9 μL of platinum-divinyltetramethyldisiloxane complex (SIP6831.2, Gelest Inc.) as catalyst, and 12 μL of 2,4,6,8-tetramethyl-tetravinylcyclotetrasiloxane as moderator (396281 Sigma-Aldrich). The volume of the moderator was increased compared to previous publications to extend the working time of the solution. The mixture was well mixed with a vortex mixer for 20 seconds, and then 0.5 g of (25-35% methylhydroxiloxane) – dimethylsiloxane copolymer, trimethylsiloxane terminated (HMS-301; Gelest Inc.) was added. The reagents were thoroughly mixed for another 20 seconds using a vortex mixer. The h-PDMS polymer is diluted with n-hexane (H303-1; Fisher) to approximately 20% w/w. This diluted solution

was vortexed for 20 seconds, followed by further homogenization on a shaker for 1 hour. A second dilution with n-hexane was necessary to obtain very dilute h-PDMS solution (0.5%, 0.75%, 1%, 1.5%, 2%, 4% w/w), similarly it was well mixed with a vortex mixer for 20 seconds and then on a shaker for 1 hour. Finally, 2700 μL of the diluted h-PDMS mixture was dispensed on the silicon SU-8 mold by low speed spin coating (WS-650-23; Laurell Technologies) using a spin recipe of 100 rpm for 10 seconds with acceleration of 100 rpm/second to spread out the solution, followed by 150 rpm for 30 seconds with acceleration of 100 rpm/second. The h-PDMS coated mold was transferred to an oven and cured at 120°C for two minutes. The mold was encased in a holder made of aluminum foil with the h-PDMS coated surface still exposed to the environment and allowed to cool. Then 25 g of PDMS (Sylgard 184, Dow Corning) at 5:1 prepolymer to cross-linker ratio was poured onto the h-PDMS mold that is encased in the aluminum foil holder. The mold with PDMS was degassed for 10 minutes and then cured at 65°C in an oven for a minimum of 6 hours. The adhesion between the h-PDMS and standard PDMS is strong enough so that both the thin film and the bulk layer can be simultaneously removed by peeling PDMS off of the mold. It should be noted that the 120°C curing step is crucial in creating the discrete h-PDMS thin film layer. Without this partial curing step, the h-PDMS will be cross-linked with the standard PDMS that is casted on top of the thin film, making the two layers indistinguishable, therefore impossible to create surface nanocracks.

In order to use the surface nanocracks in the h-PDMS as nanochannels, it is necessary to enclose the top of the nanocracks with a thin and stretchable PDMS membrane. The PDMS membrane was fabricated by first silanizing borosilicate glass slides with Tridecafluoro-1,1,2,2-tetrahydrooctyl trichlorosilane (SIT8174.0 Gelest Inc.).

Next, Sylgard 184 PDMS at 5:1 ratio was spin coated on the silanized glass slides at 500 rpm for 5 seconds with acceleration of 500 rpm/second to spread out the solution, followed by 1750 rpm for 30 seconds with acceleration of 2000 rpm/second, and cured at 120°C for ten minutes. The thickness of the resulting PDMS film was measured with a contact profilometer to be ~ 40 μm.

After the h-PDMS/PDMS material system was peeled off of the silicon and SU-8 mold, the material system was cut up into 12 mm x 42 mm pieces so that each piece contained a single device for an array of nanocracks. The h-PDMS/PDMS device was then place in a manual stretcher (MicroVice Holder; S.T. Japan USA LLC. FL, USA) and a tensile strain was applied. By applying a tensile strain, cracks initiate at the pre-patterned SU-8 notches at the top microchannel and propagate, Figure 2.1(B). Eventually the cracks terminate at the bottom microchannel to form a continuous surface crack from the top microchannel to the bottom microchannel. This pre-cracked h-PDMS/PDMS device is bonded to the 40 μm thin film PDMS with an oxygen plasma bonder (COVANCE; Femto Science Inc.) at 100 W air plasma for 30 seconds. This bonded PDMS thin film allows for the h-PDMS surface nanocracks to be used as nanochannels connecting the top microchannel to the bottom microchannel of the microfluidic device, Figure 2.2.

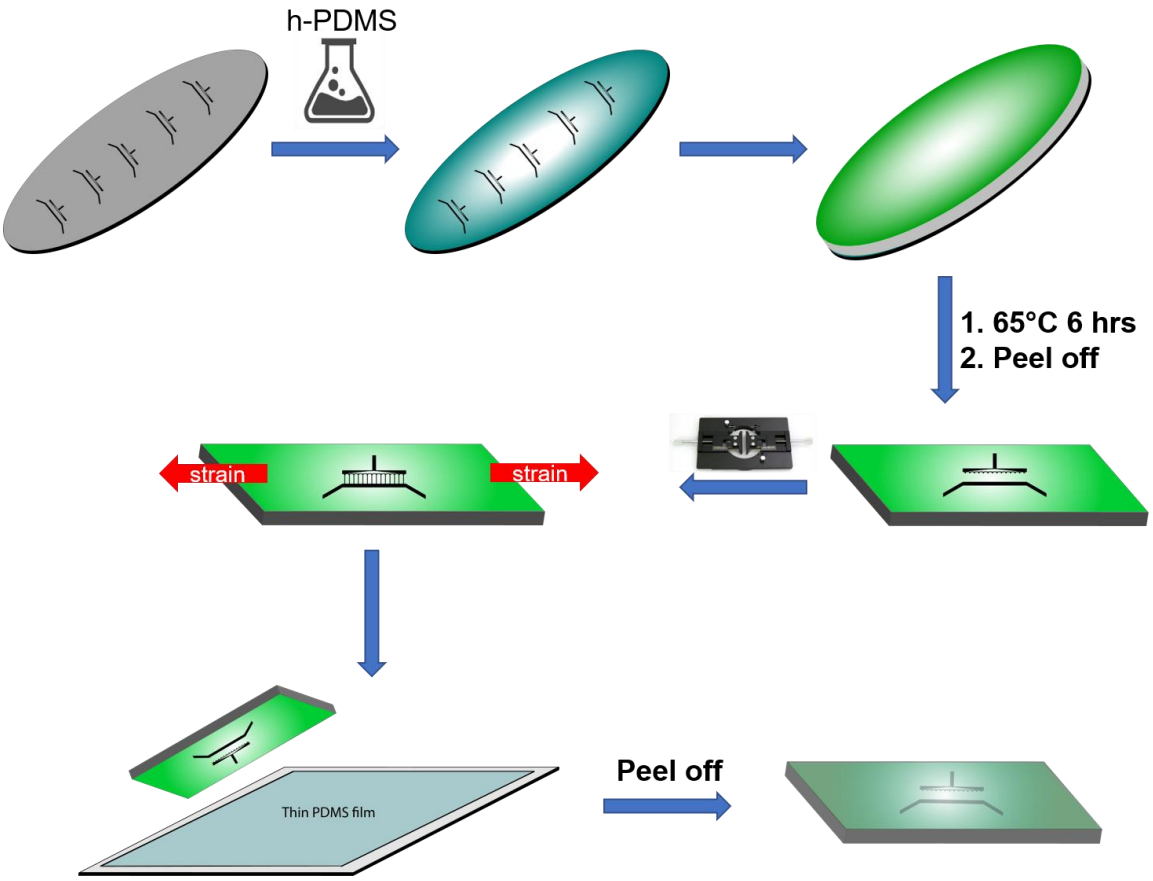

Figure 2.2 Schematics of fabrication steps for h-PDMS nanochannel devices. A thin layer of h-PDMS is spin coated on the pre-patterned silicon mold and curing at 120°C. Bulk PDMS is cast over the thin film layer and undergoes overnight curing at 65°C. The resulting h-PDMS/PDMS system is peeled off and cut into smaller pieces. Stretching with a stretcher will fracture the thin film at the pre-patterned v-notches and create cracks, when applied tensile strains are released, the cracks will heal and close. The device is bonded to a thin PDMS membrane atop of a glass slide and undergoes oxygen bonding, thereby creating PDMS membrane/h-PDMS/bulk PDMS sandwich system to seal off channels.

2.3.2 Notch design

h-PDMS thin films have been previously used to generate microcracks using a double notch design as strain relief structures (Kim et al., 2014). In this study, we investigated the placement and relative notch quantity and the implications on crack

formations. SU-8 molds were prepared featuring no notches, notches on one side, equal number of notches on both sides, and double the number of notches on one side of the microchannels. Each notch consisted of an isosceles triangle with the two equal sides at 20 μm in length and the tip of notch at 20°. The notch to notch distance in this study is 25.2 μm, and the microchannel to microchannel distance is 200 μm, Figure 2.3.

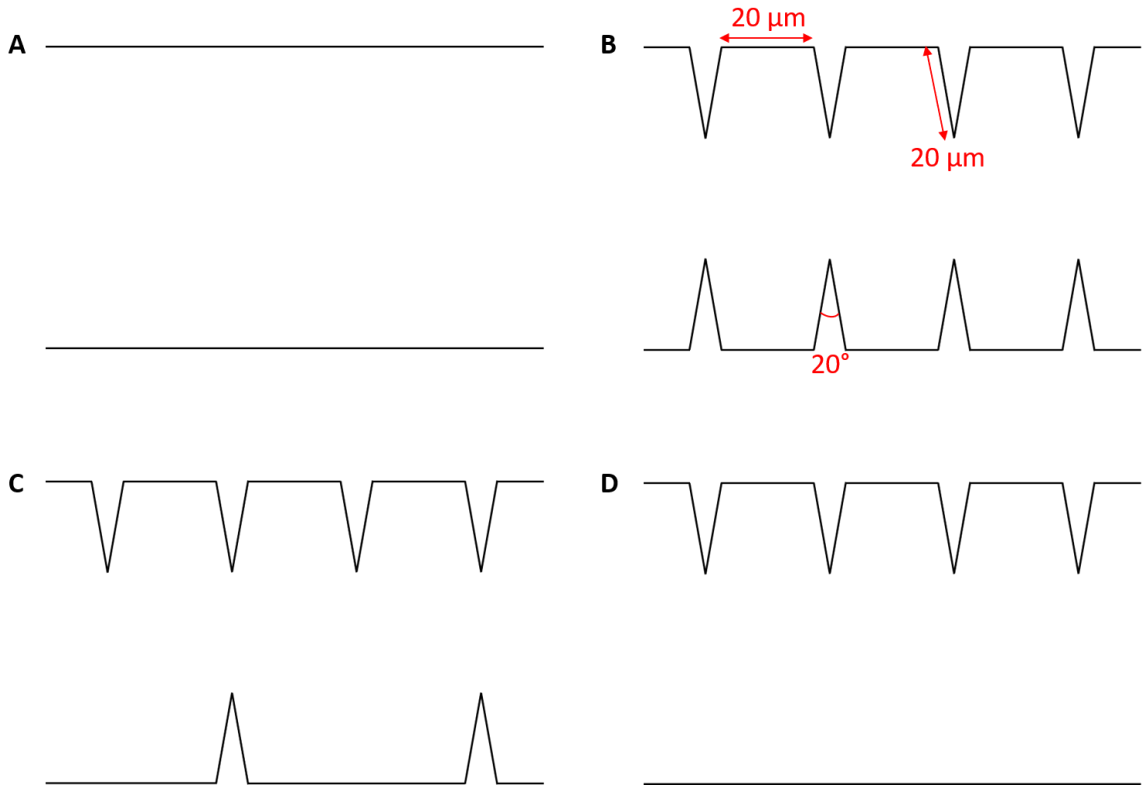

Figure 2.3 Schematic representation of v-notch design. (A) No notch along either microchannel. (B) Notches along both microchannels. (C) Double notches on one side. (D) Notches on a single side. Dimensions of the notches are as indicated in the figures, while the distance between the top and bottom microchannles can be varied, 200 μm was used specifically for this study.

2.3.3 Contact Angle measurements

SU-8 2, 2007, 2025 are spin coated and UV-exposed on silicon wafers. Measurements are gathered using the static optical tensiometry mode of a Ramé-hart Model 250 goniometer. The contact angle between different SU-8 compositions with distilled water, PDMS at 10:1 ratio, and h-PDMS without catalyst and moderator were investigated. A droplet of distilled water, and h-PDMS were deposited onto the surface using a syringe or a pipette. At precisely 10 seconds after deposition of the droplets, an optical image is acquired, and the corresponding theta angle calculated at a rate of 3 images per second for a total of 10 images. The PDMS batch was obtained by first depositing a droplet of PDMS onto the surface, cured at 120°C for ten minutes. The rest of the measurement method is the same as the DI H_2O and h-PDMS samples.

2.3.4 Thickness measurements

The relationship between the thickness of the spin coating deposited h-PDMS thin film and the dilution factor was measured with atomic force microscopy (Veeco AFM) and contact profilometry (Dektak 150 Profilometer). Tiny droplets of standard PDMS is carefully deposited on top of the h-PDMS coated mold, partially covering the SU-8 features. The system is cured at 120°C for 10 minutes, and the PDMS is peeled off removing both h-PDMS and PDMS together exposing the bare silicon substrate. Thus, the thickness of the h-PDMS layer located between the SU-8 microchannel pattern can be accessed. This is the location where future nanocracks would be located.

2.3.5 Crack depth and crack width measurements

Pre-cracked h-PDMS/PDMS slabs are mounted onto the manual stretcher and stretched with approximately 32%, 45% and 59% strain. The stretcher with the PDMS device is placed directly under the AFM probe as shown in Figure 2.5(A). The AFM cantilevers used in this study have a tip angle of 40°, tip radius 8 nm (HQ:NSC14/AL BS; μmasch).

2.3.6 DNA staining and linearization

λ-DNA was stained with YOYO-1 (Y3601; Invitrogen) at 4:1 ratio. The stained λ-DNA was diluted to 537 pg/μL in Tris-EDTA buffer. The diluted λ-DNA was loaded into the microchannel via the top inlet. A strain is applied to open the nanochannel, allowing λ-DNA to flow into the nanochannel based on hydrodynamic flow. The strain is then released to close the channel, which confines and linearizes the λ-DNA in the nanochannel. Optical images of the linearized λ-DNA were captured with Leica DMi8 at 63x oil objective with another 1.6x camera zoom.

2.4 Results and discussions

2.4.1 h-PDMS thickness

The creation of thin films of polymers by spin coating is a common fabrication technique used in cleanroom and photolithography processes such as coating silicon wafers with photoresist (Hall et al., 1998). Typically, in this spin coating process, a few milliliters of the liquid for coating is placed on the surface of a substrate, which is then brought to a rotational speed of a few 1000's of rpm. The centrifugal force causes the dispensed liquid

to spread over the surface in a uniform film, with excess liquid spun off the edge of the substrate. Additionally, the spinning causes some of the liquid's solvent component to evaporate, which slows the thinning process and stabilizes the newly formed thin film coating. In general, the attainable coating thickness is strongly dependent on the spin speed and decreases with the inverse of the square root of the spin speed (Sukanek, 1991).

Initially, this type of spin coating at high speeds (above 1000 rpm) was attempted with the hexane diluted h-PDMS but resulted in a blotchy and unusable thin film coating Figure 2.4(A). It was postulated that the coating process was dominated by the evaporation rate of the solvent and not by the spin speed as is the case for typical photoresists. This is due to the high solvent concentration of the hexane diluted h-PDMS being 98-99.5% as compared to 55-85% for common photoresists (wwwMicroChemicalscom). By plotting the thickness of the h-PDMS as a function of the dilution factor Figure 2.5(B) a linear increasing relationship is demonstrated for the h-PDMS, as opposed to the inverse relation to angular velocity for common spinnable photoresists. The thickness of the h-PDMS film is therefore controlled by the total amount of h-PDMS initially deposited onto the mold, rather than the spin speed. However, it was found that the resulting h-PDMS film is not very smooth over a large flat surface as measured by a contact profilometer and shown in Figure 2.4(B). Despite this waviness, this h-PDMS coating technique using low spin speeds is capable of creating reproducible nanoscale thickness films between the SU8 patterned crack notch features on our silicon mold. Though, we postulate for future h-PDMS formulations that by using a solvent that does not evaporate as fast as hexane, combined with faster spin coating speeds, a smoother thin film may be achieved.

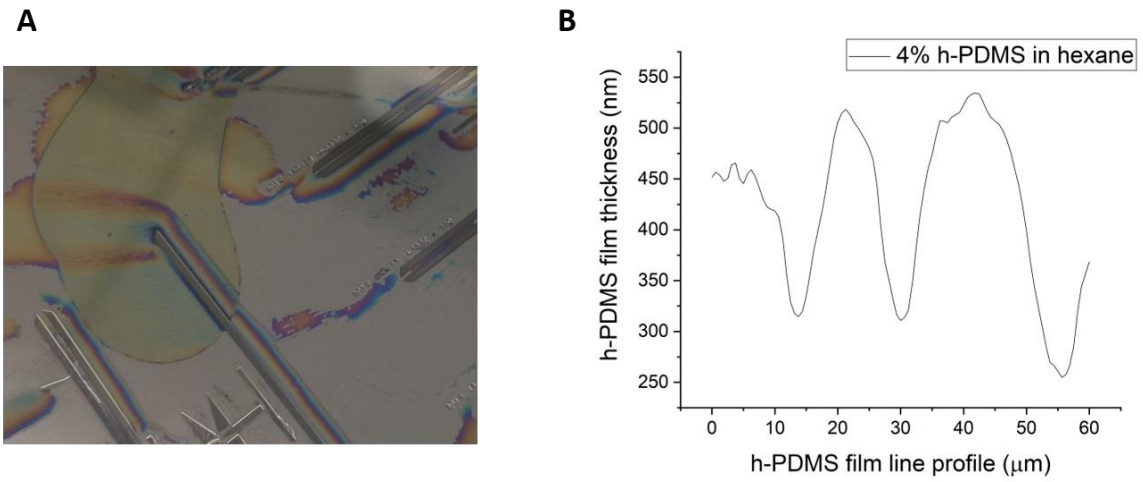

Figure 2.4 Morphology of spin coated h-PDMS. (A) Blotchy h-PDMS film on a 20 μm thick SU-8 2025 mold using high spin speed. (B) Waviness of slow speed spin coated 4% h-PDMS on a 20 μm thick SU-8 2025 across a 60 μm surface observed on profilometer.

2.4.2 h-PDMS crack depths

The purpose of the nanocracks in the h-PDMS film is to create nanochannels from them by capping the cracked surface with a thin stretchable PDMS film. These nanochannels are then used to confine and linearize DNA that flow through them. In order to increase the degree of DNA linearization, it is essential for the nanocrack (i.e. the nanochannel) depth to be minimized or to be on the order of the size of the nonlinearized DNA. Ideally, the depth of the cracks should be confined to the thickness of the h-PDMS thin film, but it is possible for the cracks to penetrate into the PDMS substrate, and therefore the crack depth will be larger than the h-PDMS thickness. Table 2.1 summarizes h-PDMS thickness due to various dilution levels and the resulting measured crack depths at different applied strains. There are two factors contributing to the observed larger values of crack depth over film thickness, the moduli mismatch between the h-PDMS/PDMS causing crack

penetration into the bulk PDMS, and the waviness in the thickness of the spin coated h-PDMS film. In a two-layer thin film system, when the crack tip originates from the stiff film, it is expected that the crack tip will penetrate into the substrate. In general, the toughness of a film decreases with increasing thickness. As the toughness mismatch between the film and substrate increases, the more likely it is for cracks to propagate into the substrate layer. This would suggest that the higher concentration of h-PDMS, i.e., a thicker film and a decreased toughness, less penetration of cracks into the substrate layer should be observed.

However, the results in Table 2.1 indicated a larger difference between crack depths and h-PDMS thickness. This is most likely due to the second factor, the waviness of the h-PDMS film. As shown in the table, the standard deviation of film thickness indicated that the waviness increases with increasing film thickness. Furthermore, a significant strain was applied to the h-PDMS/PDMS slab in order to give enough clearance for the AFM probe to facilitate the crack depth measurement, resulting in the strain energy release rate exceeding the toughness of the thicker h-PDMS, inducing undesirable crack penetrating into the bulk PDMS layer. Another factor that affects the depth of crack penetration into the substrate layer is the spacing between adjacent strain relieving notch features. By decreasing the spacing between notches, the total number of strain-relieving notches for a given device is increased, and therefore reducing the depth of individual crack penetration.

Table 2.1 Thickness (h) of h-PDMS layer on a 2 μm thick SU-8 mold and the corresponding crack depths at various applied strains. The numbers in the parentheses are the differences between the measured h-PDMS thickness and the actual crack depths.

			Crack Depths (nm)		
hPDMS (%)	h (nm)	stdev (nm)	ε=32%	ε=45%	ε=59%
0.50%	74.7	25.3	124.8 (50.1)	128.1 (53.4)	130.1 (55.4)
0.75%	145.6	17.58	207.3 (61.7)	225.2 (79.6)	229 (83.4)
1%	192.1	49.2	246.7 (54.6)	260.7 (68.6)	294.8 (102.7)
1.50%	269.5	37	412.7 (143.2)	418.4 (148.9)	NA
2%	415.9	65	506 (90.1)	485 (69.1)	NA

2.4.3 h-PDMS crack widths

In addition to crack depth, the crack width is also an important parameter to understand and characterize in order to use the nanochannels for DNA linearization. Since the nanocracks are surface cracks, the shape of the cracks is U-shaped with the maximum width occurring at the location of the h-PDMS surface, Figure 2.5 (A)&(D). The primary parameters controlling the crack width are the h-PDMS thickness and the amount of strain applied. In general, the crack width increases with increasing h-PDMS thickness and with the applied strain as demonstrated in Table 2.2. Also, it was observed that the achievable crack width is approximately within three times the maximum crack depth. Figure 2.5(D) shows the AFM measured cross-sectional profiles of typical cracks for a 1.5% diluted h-PDMS film with different applied strains. This figure demonstrates the large tuneability of the crack width, and therefore the nanochannel width, from a width of ~1 μm from an applied strain of 32% to less than 5 nm when the applied strain is removed (i.e. strain = 0%). It is this tuneability of the nanochannel width from micron scale to nanometer scale when closed, that allows the channel to be loaded with relatively large globular DNA when opened, and then highly linearize the DNA when the crack is closed. When the nanocracks

are in this closed state, they are not visible, even with optical microscopy at 100x magnification. In addition to the crack width's tuneability, the crack width is also repeatably reversible, with closed-to-open crack widths observed for over 100 cycles.

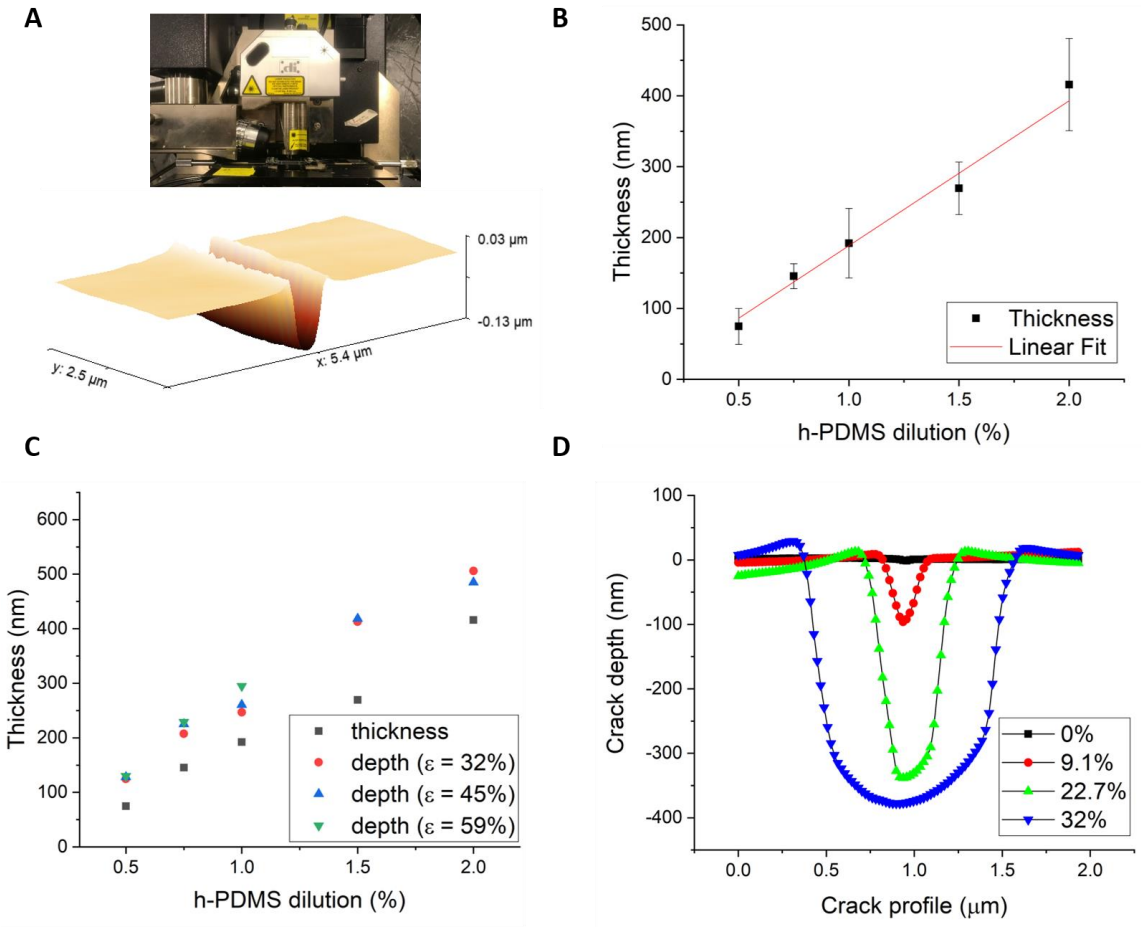

Figure 2.5 Investigation of h-PDMS thin film and crack profiles with atomic force microscopy. (A) A manual stretcher under the AFM probe, and the 3D representation of crack depth measurement of a 0.5% h-PDMS crack at 32% strain. (B) Film thickness and h-PDMS diltuion (%) plot. Thickness of h-PDMS layer exhibits a linear relationship to the percent dilution of h-PDMS solution. (C) Plot of crack depths and h-PDMS film thickness vs h-PDMS diltuion (%). Penetration of crack into the substrate PDMS layer is observed. (D) Crack profile of a 1.5% h-PDMS crack at different strain. AFM probe used in this study had a tip height of 12-18 µm and a tip radius of 8 nm.

Table 2.2 Crack widths (μm) and at corresponding applied strains. Widths of cracks increases with increasing strain.

hPDMS dilution	ε=32%	ε=45%	ε=59%
0.5%	0.37	0.45	0.46
0.75%	0.56	0.65	0.67
1%	0.725	0.74	1.05
1.5%	1.08	1.26	
2%	1.37	1.48	

2.4.4 Saw tooth V-notch design and crack generation

Crack formations on the no-notch case are driven by intrinsic defects in the h-PDMS system, the cracks are therefore generated at random, Figure 2.6(A). In the case where notches are located on both sides of the microchannels, cracks can initiate on either side at the tips of the notches. This method was demonstrated and used in creating microcracks in literature (Kim et al., 2014). However, the cracks would not necessarily reach the tips of the notches on the opposite side. This is most often observed when cracks initiations begun from both opposing notches. As the crack neared the opposite notch, the local strain nearby was released by the crack initiated at this opposite notch, therefore preventing the crack from propagating further, Figure 2.6(B).

The notch patterns are designed to shield intrinsic defects while leaving only the tip of the notch as the strain focusing points to initiate cracks. As the number of cracks increases, the spacing between each artificial defect decreases, a higher strain would therefore be required to initiate cracks. It is postulated that cracks would preferentially initiate on the side with lower number of notches. However, as shown in Figure 2.6(C),

doubling the number of notches is not enough to achieve the desired effect. Although cracks preferentially initiated at the side with lower number of notches, the side with higher number of notches was also activated as we continue to increase strain to help crack propagations, as characteristic spacings will decrease with increasing applied strain. This is due to the spacing between notches in this design is still within the regime where crack formation can be activated, higher number of notches are therefore required to shield the strains. Instead of patterning more notches, this undesirable behavior can be eliminated by single notch side pattern, as increasing the number of shielding features would eventually equate to zero notches. The cracks are initiated on the side with the notch pattern, and propagate all the way to the bottom microchannel to create through cracks, Figure 2.6(D). This pattern is preferred when patterning parallel cracks at discrete spacing.

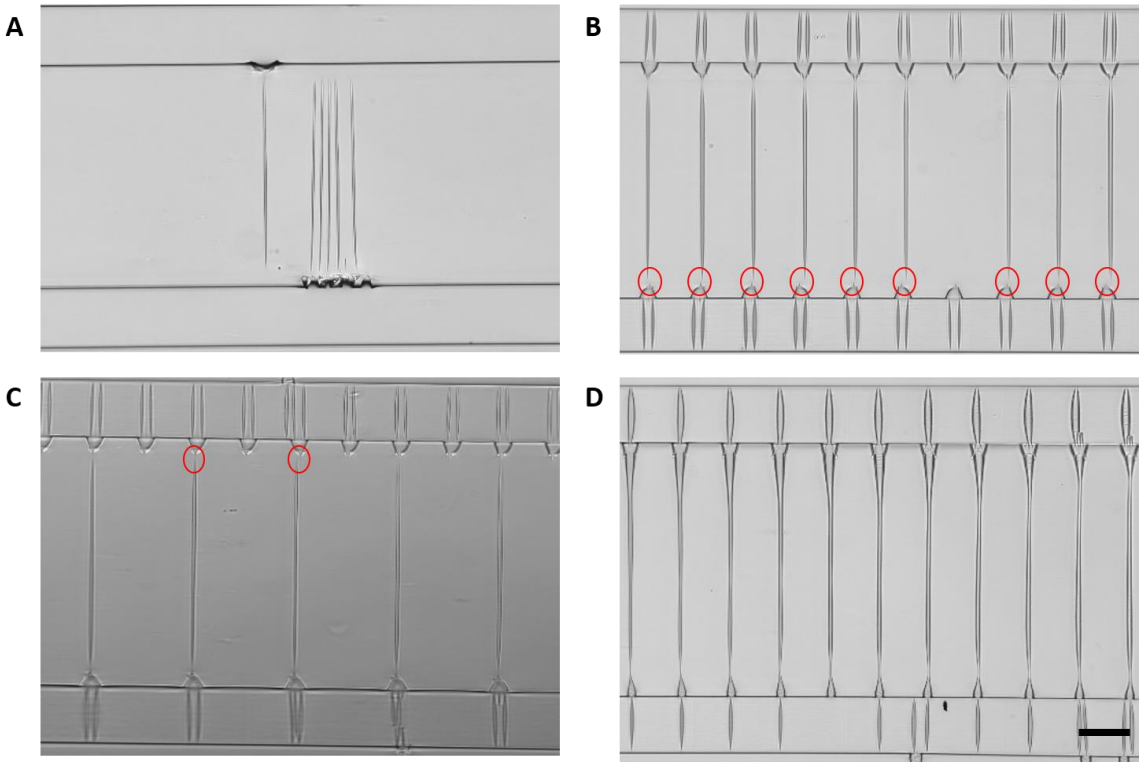

Figure 2.6 Optical images of different v-notch design. Red circles indicating prematurely terminated cracks. Scale bar = 50 μm. (A) No notch pattern where stochastic cracks are observed. (B) Equal notches along both microchannels (C) Notches along both microchannels, with one side doubling number of notches. (D) Notches on only one of the microchannels.

2.4.5 h-PDMS and SU-8 mold thickness

At a glance, the distribution of h-PDMS on SU-8 mold appeared to be dependent on the thickness of pre-patterned SU-8 features. Figure 2.7 illustrated the changes in the thickness of spin coated h-PDMS between the two microchannels. When the height of the SU-8 feature is 2 μm thick, the thickness of h-PDMS layer is the thickest near the edge of the microchannel, and progressively decreases in thickness as it nears the center of the channel. *Vice versa* in the case a 20 μm SU-8 mold, the center region is the thickest and

thins out near the edge of the microchannel. It is worth noting that Figure 2.7(A) eventually leveled out as the probe moved across the h-PDMS thin film towards the center of the mold, but is cropped to the same scale as Figure 2.7(D) for easier comparison. The edge thinning feature of the thicker SU-8 mold is further illustrated in the AFM crack profile. The three horizontal lines in Figure 2.7(H) correspond to the crack profiles in Figure 2.7(I). We found that both the widths and the depths of a h-PDMS crack fabricated using the 20 μm SU-8 mold progressively narrowed and became shallower near the edge of the microchannel.

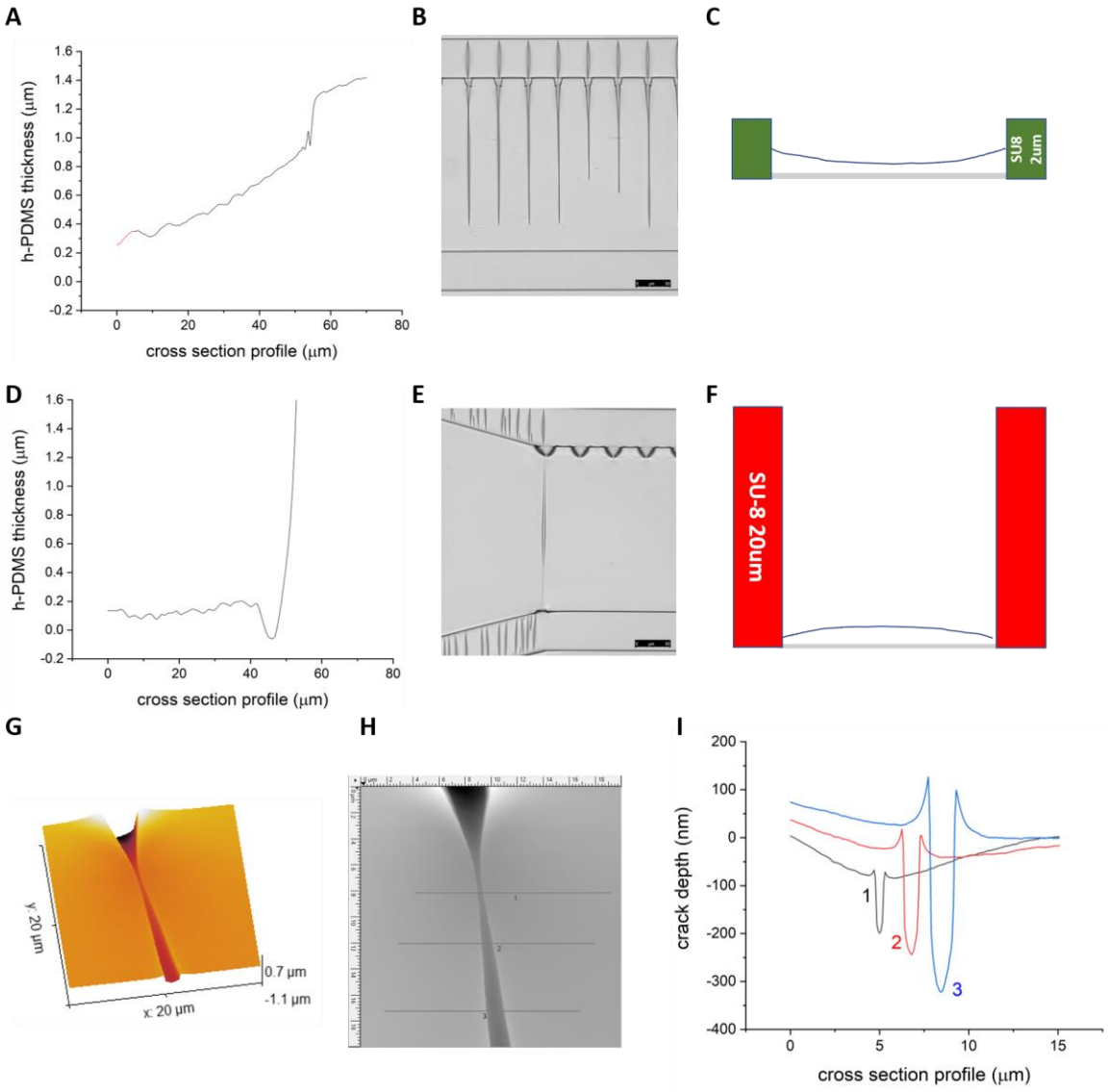

Figure 2.7 Distribution of h-PDMS on varying heights of prepatterned SU-8. (A) Profilometer profile of h-PDMS layer from center to 2 μm SU-8 feature. (B) Optical images of crack formations from a 2 μm SU-8 mold, scale bar = 50 μm. (C) Exaggerted schematic representation of h-PDMS thickness distribution. (D) Profilometer profile of h-PDMS layer from center to 20 μm SU-8 feature, scale bar = 50 μm. (E) Optical images of crack formations from a 2 μm SU-8 mold. (F) Exaggerted schematic representation of h-PDMS thickness distribution. (G) AFM 3D representation of the edge of a crack fabricated from 2 μm SU-8 mold. (H)&(I) Crack depth and crack width results of corresponding line profile.

However, the SU-8 height is not the only contributing factor to the thickness distribution. The concentration of the h-PDMS solution also plays a role, Figure 2.8, and the distribution further affects the morphology of the cracks resulting in different behaviors when opening and closing of pre-cracked h-PDMS system. When the SU-8 to h-PDMS ratio is low, the crack opens from the edge at the notch side. The widths of the cracks are visibly wider near the edge of the microchannels and narrower in the middle sections of the cracks. Whereas the opposite is observed when the SU-8 to h-PDMS thickness ratio is high, the crack is the widest in the mid-section of the cracks. We postulate that this behavior would imply varying difficulties to load biopolymers into the crack channels with the low SU-8 to h-PDMS easier for loading.

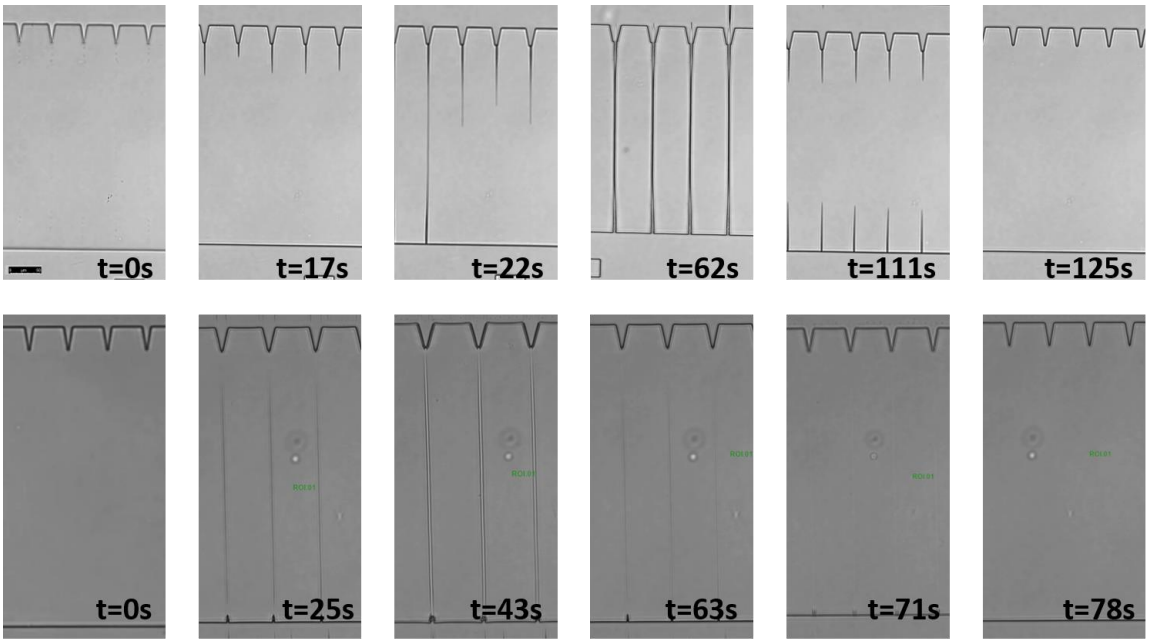

Figure 2.8 Optical images showing contrasting behaviors of opening and closing of cracks made from 2 µm SU-8 with 1 µm h-PDMS thickness (top row) vs. 120 nm h-PDMS thickness (bottom row).

2.4.6 Contact angle and h-PDMS distributions

It is postulated that the distributions of the h-PDMS may be a result of varying wetting behaviors of h-PDMS solution on SU-8 photoresist, therefore the contact angles of different compositions of SU-8 were investigated. Table 2.3 compiled the different contact angles with water, PDMS and h-PDMS. A progressively hydrophobic behavior, higher theta angle, is observed in all three type of liquids. This result indicates that as the dilute h-PDMS solution was spin coated onto the mold, the SU-8 2025 mold would repel h-PDMS more, therefore potentially driving the h-PDMS away from the SU-8 feature. Conversely, the SU-8 2 molds would allow easier wetting of the surface, therefore the h-PDMS layer could be more evenly distributed onto the surface. The precise dynamics and spin coating of a thin polymer film is very complex, but here we provide a potential explanation for our observations to why differing distributions of h-PDMS layers are observed with the same deposition method.

Table 2.3 Contact angle of different SU-8 compositions. Contact angle increases with higher numbering, thicker film, SU-8 species.

	SU8-2	SU8-2007	SU8-2025
H_2O	66.9	74.3	83.1
PDMS	30	45.3	51
h-PDMS	27.3	36.6	60.3

2.4.7 Lambda DNA linearization

Table 2.4 summarizes the results of λ-DNA linearization. The distribution of degrees of extension was processed with ImageJ. A total of 112 pieces of DNA molecule were counted. Contour length 22 μm was assumed for this base pairs to dye ratio for λ-DNA (Kundukad et al., 2014). Compared to oxidized PDMS nanochannel, we observed a lower number of fully extended DNA at 18.8% to 34.8%. It is important to note that in the oxidized PDMS studies, a recipe of multi-steps slow relaxation of nanochannels to their closed state, with a further -0.5% strain squeezing of nanochannels to linearize DNA was utilized (Matsuoka et al., 2012). It was postulated that the speed of closing nanochannel can affect DNA extension (Han et al., 2016). In this current study, h-PDMS nanochannels were closed from 100% strain to 0% in 1 step at 1 mm/sec speed. It may be possible to increase the degrees of linearization by implementing a slow speed squeezing method with h-PDMS system.

Table 2.4 Percent DNA extension in h-PDMS nanochannel compared to oxidized PDMS nanochannel (Matsuoka et al., 2012)**.**

Extension	Oxidized PDMS	hPDMS
<40%	33.5%	35.7%
40-60%	9.5%	24.1%
60-80%	21.8%	18.8%
80-100%	34.8%	18.8%
100% - 115%	NA	2.6%

2.5 Conclusion

Despite the interest in utilizing physical confinement of nanochannels to analyze linearized DNA molecules, realistically the fabrication of nanochannels and localization of

DNA can be challenging. Conventional lithographic fabrication-based nanochannel are restricted by fixed channel dimensions. Our previous iteration of fractured based nanochannel fabrication relies on inherent defects existing in oxidized PDMS. The fracture process can start randomly from any defect and the depth of the nanochannel is difficult to control because the depth of plasma oxidation of PDMS is not well characterized.

Utilizing the same principle as the two-layered fracture system, h-PDMS can substitute as the stiff layer. By implementing a pattern where the strain shielding notch features locate only on one side, we're able to consistently reproduce through cracks that can be utilized as through channels. Due to the reversible nature of these h-PDMS nanocracks, DNA can be loaded and linearized. Computer simulations modeled the squeezing-induced hydrodynamic flow of tunable oxidized PDMS nanochannels and found that the initial extension plays an important role to the ultimate achievable linearization length (Han et al., 2016). However, it was also shown that a rate dependent application of opening and closing of channels was conducive to further extension with it being most effective on initial extension contour length. Combined with a controlled stretcher system, the h-PDMS nanochannels would be an effective system for consistent DNA linearization. The scalable potential of this h-PDMS thin film coating method provides flexible regime for different biological applications and not just biopolymer linearization.

2.6 References

Beuth, J.L. (1992). Cracking of thin bonded films in residual tension. Int. J. Solids Struct. *29*, 1657–1675.

Bilenberg, B., Jacobsen, S., Schmidt, M.S., Skjolding, L.H.D., Shi, P., Bøggild, P., Tegenfeldt, J.O., and Kristensen, A. (2006). High resolution 100 kV electron beam lithography in SU-8. Microelectron. Eng. *83*, 1609–1612.

De Carli, F., Menezes, N., Berrabah, W., Barbe, V., Genovesio, A., and Hyrien, O. (2018). High-Throughput Optical Mapping of Replicating DNA. Small Methods *2*, 1800146.

Cho, Y.H., Park, J., Park, H., Cheng, X., Kim, B.J., and Han, A. (2010). Fabrication of high-aspect-ratio polymer nanochannels using a novel Si nanoimprint mold and solvent-assisted sealing. Microfluid. Nanofluidics *9*, 163–170.

Douville, N., Huh, D., and Takayama, S. (2008). DNA linearization through confinement in nanofluidic channels. Anal. Bioanal. Chem. *391*, 2395–2409.

Hall, D.B., Underhill, P., and Torkelson, J.M. (1998). Spin coating of thin and ultrathin polymer films. Polym. Eng. Sci. *38*, 2039–2045.

Han, M., Kim, B.C., Matsuoka, T., Thouless, M.D., and Takayama, S. (2016). Dynamic simulations show repeated narrowing maximizes DNA linearization in elastomeric nanochannels. Biomicrofluidics *10*, 064108.

Huang, J., Kim, B.C., Takayama, S., and Thouless, M.D. (2014). The control of crack arrays in thin films. J. Mater. Sci. *49*, 255–268.

Huh, D., Mills, K.L., Zhu, X., Burns, M.A., Thouless, M.D., and Takayama, S. (2007). Tuneable elastomeric nanochannels for nanofluidic manipulation. Nat. Mater. *6*, 424–428.

Kim, B.C., Matsuoka, T., Moraes, C., Huang, J., Thouless, M.D., and Takayama, S. (2013). Guided fracture of films on soft substrates to create micro/nano-feature arrays with controlled periodicity. Sci. Rep. *3*, 3027.

Kim, B.C., Moraes, C., Huang, J., Matsuoka, T., Thouless, M.D., and Takayama, S. (2014). Fracture-based fabrication of normally closed, adjustable, and fully reversible microscale fluidic channels. Small *10*, 4020–4029.

Kundukad, B., Yan, J., and Doyle, P.S. (2014). Effect of YOYO-1 on the mechanical properties of DNA. Soft Matter *10*, 9721–9728.

L. Jay Guo, *,†, Xing Cheng, † and, and Chia-Fu Chou*, ‡ (2003). Fabrication of Size-Controllable Nanofluidic Channels by Nanoimprinting and Its Application for DNA Stretching.

Lam, E.T., Hastie, A., Lin, C., Ehrlich, D., Das, S.K., Austin, M.D., Deshpande, P., Cao, H., Nagarajan, N., Xiao, M., et al. (2012). Genome mapping on nanochannel arrays for structural variation analysis and sequence assembly. Nat. Biotechnol. *30*, 771–776.

Mannion, J.T., Reccius, C.H., Cross, J.D., and Craighead, H.G. (2006). Conformational Analysis of Single DNA Molecules Undergoing Entropically Induced Motion in Nanochannels. Biophys. J. *90*, 4538–4545.

Matsuoka, T., Kim, B.C., Huang, J., Douville, N.J., Thouless, M.D., and Takayama, S. (2012). Nanoscale squeezing in elastomeric nanochannels for single chromatin

linearization. Nano Lett. *12*, 6480–6484.

Mills, K.L., Zhu, X., Takayama, S., and Thouless, M.D. (2008). The mechanical properties of a surface-modified layer on poly(dimethylsiloxane). J. Mater. Res. *23*, 37–48.

Mills, K.L., Huh, D., Takayama, S., and Thouless, M.D. (2010). Instantaneous fabrication of arrays of normally closed, adjustable, and reversible nanochannels by tunnel cracking. Lab Chip *10*, 1627–1630.

Reccius, C.H., Mannion, J.T., Cross, J.D., and Craighead, H.G. (2005). Compression and Free Expansion of Single DNA Molecules in Nanochannels. Phys. Rev. Lett. *95*, 268101.

Riehn, R., Lu, M., Wang, Y.-M., Lim, S.F., Cox, E.C., and Austin, R.H. (2005). Restriction mapping in nanofluidic devices. Proc. Natl. Acad. Sci. U. S. A. *102*, 10012–10016.

Sukanek, P.C. (1991). Dependence of Film Thickness on Speed in Spin Coating. J. Electrochem. Soc. *138*, 1712.

wwwMicroChemicalscom Composition and Properties of AZ® and TI Photoresists.

Zhu, X., Mills, K.L., Peters, P.R., Bahng, J.H., Liu, E.H., Shim, J., Naruse, K., Csete, M.E., Thouless, M.D., and Takayama, S. (2005). Fabrication of reconfigurable protein matrices by cracking. Nat. Mater. *4*, 403–406.

CHAPTER 3. ON-MICROSCOPE UNIAXIAL STRETCHING DEVICE FOR WIDTH CONTROL OF H-PDMS CHANNELS ACTING AS FEMTOLITER -VALVES

3.1 Abstract

As integrated fluidic structure continued to downscale and increase in complexity, there is a need to invest in platforms that are capable of femtoliter fluid volume control. An automated stepper motor-based stretcher with precise microscale control was designed to manipulate the h-PDMS/PDMS crack channels. In this study, we investigated the precision of the stretcher with and without a load, and the drift that occurred as the load was maintained at different strains. We found the precision to be below ±0.5 μm and the drift to be independent of applied strain but with experiment time. Combined with the crack channels, the stretcher controls the widths and the closing/widening motion of the channels by varying applied strains and the channel openings can serve as valves, observing 280 fL s^{-1} flow rate. The computer program-controlled stretcher allowed for cyclic motions and demonstrated the robustness of the system with over 100 cycles of the open/close operations.

3.2 Introduction

Over the past decade, microfluidics devices with precise control and manipulation of fluids in and below the micron scale have revolutionized the research landscape of multiple disciplines (Lin et al., 2018; Napoli et al., 2010). The use of microfluidic technology also came with green technology implications where the system is capable of reducing costs in

both labor and materials, and the reduction of hazardous waste, therefore attractive as a prototyping platform. The modern microfluidics designs may combine photonics (Godin et al., 2008), acoustic (Strohm et al., 2019), thermopneumatic (Selvaganapathy et al., 2003) or electronics (Hamedi et al., 2016) system to facilitate various fluid operations. As the field matures, the systems have become more complex to match multidisciplinary needs.

One key component in fluid control is the valving system (Thorsen et al., 2002). The predominant microfluidic valving system is pressure driven, utilizing an actuator to physically deform a top layer by applying a pressure from the z-axis to decrease flow rate to exert nanoliter scale volume control (Studer et al., 2004). Such methodology had been applied onto soft materials system such as PDMS microfluidic devices (Douglas B. Weibel et al., 2005; Unger et al., 2000), and also glass based devices for use with more aggressive chemical solutions (Kazoe et al., 2019). Another method is through the use of surface modification to achieve valving (Mawatari et al., 2012; Yang, 2011). However, as the field continues to scale down and explored the realm of nanofluidic, control for volumes in the range of pico-, and femto- scale is needed.

An automated stretcher was designed to take advantage of the tunable crack channels system, a normally closed microfluidic device based on thin film fracture in a multilayer elastomeric system capable of variable channel widths with the use of an applied strain (Kim et al., 2014). The stretcher is capable of micron scale movement, which in turn allows us to perform fine control over crack channel widths, while without an applied strain, the channels would return to a completely closed state, thereby eliminating any fluidic flow. The z-dimension of the channel is determined by film thickness which is easily tuned by spin-coating process with thickness ranging from 100 nm to 10s of microns, bypassing

traditional nanochannel fabrication techniques (Chen and Zhang, 2018). These channels can act as valves for fluidic control, eliminating the need for complex nanolithography methods. This stretcher/crack channel system also avoids the pitfalls of a pressure-driven flow design where the thin, deformable layer PDMS may collapse and experience loss of fluid control.

3.3 Materials and methods

3.3.1 Stretcher setup

The stretcher device is custom designed and fabricated in order to fit on top of an inverted microscope to allow for *in situ* high magnification viewing of test samples during uniaxial stretching. The stretcher is comprised of two compact linear actuators (DRSM60-05A4AZMK; Oriental Motor), two actuator drivers (AZD-KD; Oriental Motor), power supply unit (XG4; Advanced Energy), a computer with a MATLAB-based custom GUI to control the actuators, and the stretcher mechanism. The entire device rests on top of a microscope stage (DMi8; Leica Camera AG) and fits within the microscope stage insert to hold the base of the device stationary relative to the stage. The stretcher mechanism is predominantly machined from 6061 aluminum, with the base being the largest component. Test samples (e.g. PDMS nanochannel device) that are to be stretched, are compression clamped on opposite sides of the sample to the sample holder arm. Each of the two sample holder arms have two linear bearings that fit on two cylindrical steel guide rails. The linear bearings and guide rails constrain the movement of the sample holders and allow them to only move parallel to each other. Each sample holder arm is attached to the lead screw of a linear actuator. The use of two linear actuators allows for increased control of how the

test sample is uniaxially stretched. By moving the actuators in equal and opposite directions the region of interest being viewed at high magnification remains stationary. This allows for specific nanocracks to be viewed live while a tensile strain is applied and subsequently relieved. Conversely, if only one actuator is used, the nanocracks would move out of the microscopic field of view in the direction of the actuator. Additionally, the two actuators can be moved in different amounts to move a specific crack within the field of view. These specific linear actuators were chosen due to their maximum force capability of 500 N, their ability to hold that maximum load for extended periods of time, and their high resolution. Depending on the type of material or device being tested in the stretcher, the required force may be very high (~180 N for a microfluidic hPDMS/PDMS nanochannel/nanocrack device). Additionally, the actuators have a factory default resolution of 1 µm but can be enhanced to 0.4 µm if needed through the controlling software.

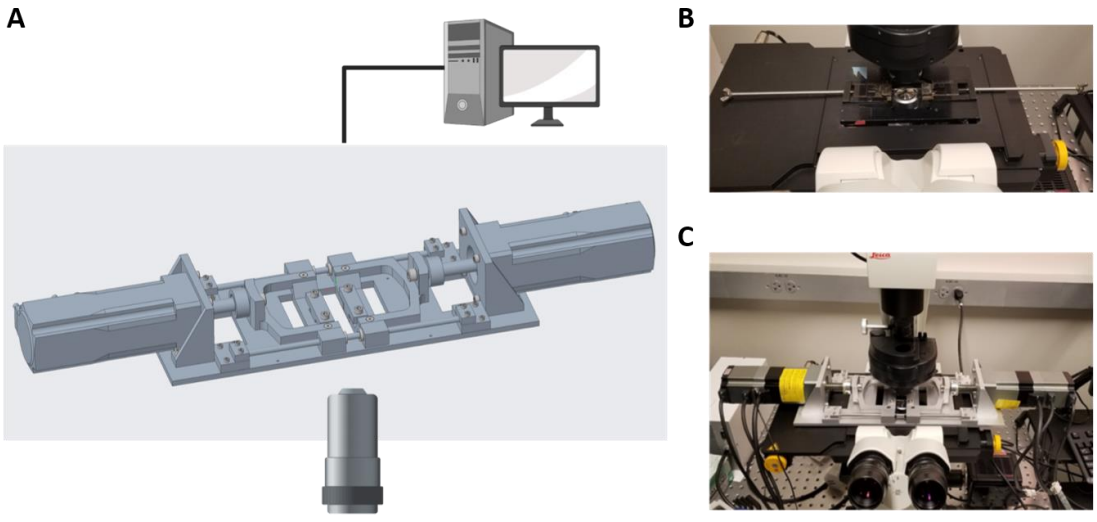

Figure 3.1 Stretcher setups. (A) Schematic representation of automated stretcher setup. (B) Manual stretcher setup. (C) Automated stretcher on a Leica DMi8 microscope sample holder.

3.3.2 Tunable h-PDMS cracks

The microchannel mold was fabricated using standard photolithography processes including a maskless aligner (MLA150; Heidelberg Instruments). The v-notch pattern was fabricated on a silicon wafer with SU-8 2007 (Microchem) as the negative photoresist with a channel height (i.e. photoresist thickness) of 7 μm following the manufacturer recommended spin coating recipe. Figure 3.2 illustrated the design of the microchannel. The top and bottom microchannels are 3 mm in length, channels widths at 60 μm. The v-notch along the top microchannel denotes the crack initiation spots, and each notch is an isosceles triangle with 20 μm sides and 20° angle at its tip.

Diluted h-PDMS was prepared with 1.7 g of (7.0-8.0% vinylmethylsiloxane) – dimethylsiloxane copolymer, trimethylsiloxy terminated (VDT-731; Gelest Inc.), 9 μL of platinum-divinyltetramethyldisiloxane complex (SIP6831.2; Gelest Inc.) as the catalyst, and 12 μL of 2,4,6,8-tetramethyl-tetravinylcyclotetrasiloxane as the moderator (396281 Sigma-Aldrich) followed by dilution with n-hexane (H303-1; Fisher) to 4%. The diluted h-PDMS solution was deposited onto the SU-8 mold via a slow speed spin coating process at 100 rpm for 10 seconds with an acceleration of 100 rpm/second to spread out the solution, followed by 150 rpm for 30 seconds with an acceleration of 100 rpm/second, and then cured at 120°C for 2 minutes. The resulting h-PDMS film is has a thickness of 600 to 800 nm. Twenty-five grams of bulk PDMS (Sylgard-184; Dow Corning) with a 5:1 ratio was cast on top of the h-PDMS coated SU-8 mold and then cured overnight in a 65°C oven. The h-PDMS/PDMS system is peeled off of the SU-8 mold and then the individual future nanofluidic devices are cut into multiple 40 mm by 12 mm pieces. Each device is clamped onto the stretcher device for pre-cracking. Approximately 100% strain is required to initiate

surface cracks in the h-PDMS thin film that are orthogonal to the direction of the applied strain. The cracks begin at the v-notch tip on the side of the top microchannel and propagate to the bottom microchannel. When the strain is removed, the cracks are relaxed and closed. This pre-cracked h-PDMS/PDMS device is bonded to a 120 μm thin film of PDMS with an oxygen plasma bonder (COVANCE; Femto Science Inc.) at 100W air plasma for 30 seconds. This bonded PDMS thin film allows for the h-PDMS surface nanocracks to be used as nanochannels connecting the top microchannel to the bottom microchannel of the microfluidic device.

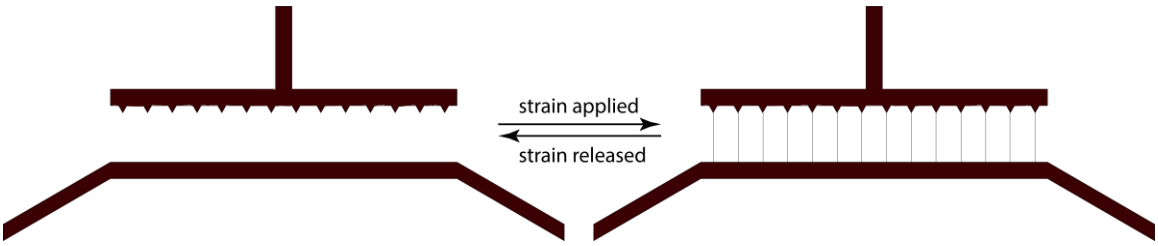

Figure 3.2 Schematic of stretcher operations to open and close channels. Not drawn to scale.

3.3.3 Stretcher calibration without load

The motors that drive the linear actuators are stepper motors equipped with a built-in mechanical absolute encoder giving closed-loop positional feedback for precise rotor rotation. The motor driver takes in commands from a computer via serial communication, and converts to pulses used to initiate rotor rotation. The accuracy and precision of the stretcher were studied by varying the motor displacement step size and motor speed. The effect of the displacement size was investigated by changing the actuator step size from 1

μm to 5000 μm per step at a fixed speed of 1 mm/s. The effect of the motor speed of the motor was evaluated by varying the speed between 10 μm/s and 2 mm/s for a set of several displacement step sizes.

The waveform analyzer provided by Oriental Motor was used as built-in encoder of the actuator providing real-time states of the motors, and the speed of the motor is controlled by a closed loop system. The actual motor displacement was calculated from rotations in degrees obtained by the waveform analyzer. Bright field images (at 64X magnification) taken from DMi8 have been processed and calculated by tracking the averaged-out edge movement in pixels using MATLAB.

3.3.4 Stretcher calibration with strain

We used an optical method to quantify slipping drift over time with loading applied. A 3.35-mm thick, 40-mm long PDMS slab labeled with a sharpie was placed onto the stretcher guide, tightly gripped on both sides. At each experiment, the slab was stretched by 1 mm, and 10 mm (6.41% and 64.1% strain respectively) in total, and then was held at the same strain for 20 minutes. Using the edges of two lines left by the sharpie, we measured the changes in distance. Bright field images were taken at every 10 seconds interval. The procedures were repeated three times without removing the slab between each of the three trials.

3.3.5 Femtoliter valve

A pre-cracked h-PDMS/PDMS slab is bonded to a 120 μm PDMS membrane with an oxygen plasma bonder (COVANCE; Femto Science Inc.) at 100W air plasma for 30

seconds, sandwiching the h-PDMS layer in between. When an external strain is applied to the device, channels will form where the cracks were. The width of the cracks can be adjusted to different sizes by the amount of strain applied. In this study, three different channel sizes were implemented, 750 nm (sub-micron), 1 μm (narrow) and 2.5 μm (wide).

With the ability to precisely control the opening and closing of channels, these crack channels can serve as nano-valves in microfluidic devices. The top and bottom inlet ports of the microchannels are connected to an EVEFLOW pump, which controls the fluidic pressure in the large microchannels. Sulforhodamine dye (1 mg/mL) is introduced into the channel from the top inlet port at 30 or 40 mbar, while distilled water is pushed through the bottom microchannel to flush out dye at 10 or 20 mbar. The opening and closing of the crack channels are controlled by the stretcher at 1 mm/s speed. After every opening, the channels are left open for 5 secs. Similarly, the crack channels are left closed for 5 secs to allow sufficient time for the bottom channels to be flushed by DI water and recover to its no fluorophore state.

3.4 Results and discussions

3.4.1 Motor calibration without load

In order to confidently use this stretcher device to measure microscale deformations and crack widths it is necessary to characterize the observed sample output displacement for a given input displacement. Factors that could potentially affect this include the input displacement magnitude and actuator speed. Additionally, it is possible for the actuators to provide different output displacements in a loaded scenario (ex. actuator moving with clamped nanochannel device to stretch) verse an unloaded scenario (ex. actuator moving

without a nanochannel device to stretch). The effect of these parameters was investigated and are discussed subsequently.

To investigate the effect of input displacement magnitude on the accuracy of the output displacement, a range of input displacements was tested (1, 5, 10, 20, 50, 75, 500, 750, 1000, 2000, 5000 μm) and the resulting output displacement was measured. These tests were performed without a nanochannel device being stretched, and therefore the apparatus was in the unloaded configuration. It was observed that small input displacements had similar differences between the input displacement and measured output displacement (Δ displacement) as larger input displacements. The average Δ displacement values were smaller than ±0.5 μm for all input displacements, with the smallest Δ displacement resulting from the smallest input displacement. This was unexpected, but is a more ideal behavior, where the stretcher output displacement is not strongly dependent on the magnitude of the input displacement. These measured errors are most likely due to random noise, and fall within the stated error of ±0.555 μm given by the stepper motor manufacturer.

In addition to displacement magnitude, the effect of varying the actuator speed was investigated. For the same range of input displacements (1, 5, 10, 20, 50, 75, 500, 750, 1000, 2000, 5000 μm), the resulting output displacements were measured using an actuator speed of 1000 μm/s and 2000 μm/s. The output displacement was measured using high magnification optical microscopy as well as an optical encoder integrated into the linear actuator. These measurements showed no significant difference in the Δ displacement over the range of input displacements using either optical microscopy measurements or the optical encoder. The measured Δ displacement for all the cases were within the stated error

of ±0.555 µm given by the stepper motor manufacturer. The optical microscopy methods gave a slightly higher mean Δ displacement, but this is believed to reflect the limitation of optical imaging, rather than a true representation of the error of motor movements.

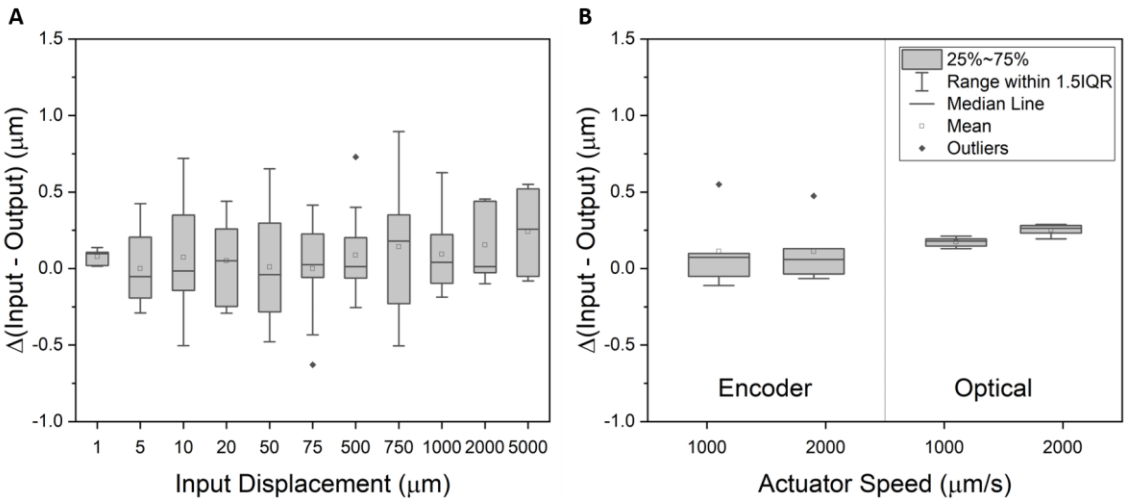

Figure 3.3 Box plots of displacement accuracy without load. (A) Displacement by step size at 1 mm/s. (B) Displacement by speed at 1000 and 2000 µm/s; Input displacement = 1000 µm, recorded with both optical and electrical encoder. Both sets of experiments were performed 10 times and less than ±0.555 µm differences between input and output was observed.

3.4.2 Stretcher calibration with strain

When performing uniaxial tension tests on materials, it is common to apply a given strain to the test sample and hold it for an extended time. This can be for performing viscoelastic characterization or for observation of the test material while loaded. In this specific case, it is desired to apply a tensile load to the PDMS nanochannel device to open the nanochannels wide and allow liquid to flow through them. Then when it is desired to stop flow, remove the tensile strain and nanochannels will close. Therefore, it is necessary

to characterize the amount of slip or drift that the test sample may experience while strained. This slip or drift can be caused by the grips not holding the test sample completely, the stepper motors that drive the linear actuators' inability to remain completely stationary, or miscellaneous slack in the stretcher mechanism.

The first set of experiments to characterize the stretcher systems slip consisted of applying a strain of 64.1% to a 40-mm-long PDMS nanochannel device at a speed of 1 mm/s. This strain was then attempted to be held for 20 min, during which, optical measurements of the location of the markings on the PDMS device were recorded every 10 seconds. After 20 minutes, the strain of the PDMS was returned to 0%, and then the test was repeated for a total of 3 trials. These measurements of local Δ width of between two markings over time are shown in Figure 3.3A for a strain of 64%, and the total Δ width for each trial for 64.1% and 6.40% strain is summarized in Table 3.1. The larger sample strain of 64.1% resulted in larger slip than the 6.40% strain case due to higher axial forces, as is expected if slip is present in a system. Additionally, the first trial for each series of experiments at different strain levels resulted in the greatest slip. Then, trials two and three had significantly less slip, where trial three for both strain levels of 64.1% and 6.40% had 50 nm and 33.3 nm of slip respectively. This slip of the final trial was extremely small and less than the optical limitation at the 64x total optical magnification used. Additionally, the effect of actuator speed on measured slip was investigated by testing four combinations of high speed (10 mm/s), low speed (0.1 mm/s), high strain (50%), and low strain (8%) (Figure 3.3B-E). It was observed that high speeds significantly reduce the measured slip the test sample experiences. In general, the slip/drift of this stretcher machine is not

significantly large, but it can be minimized and managed by using higher actuator speeds and at least two tensile cycles before beginning device experiments.

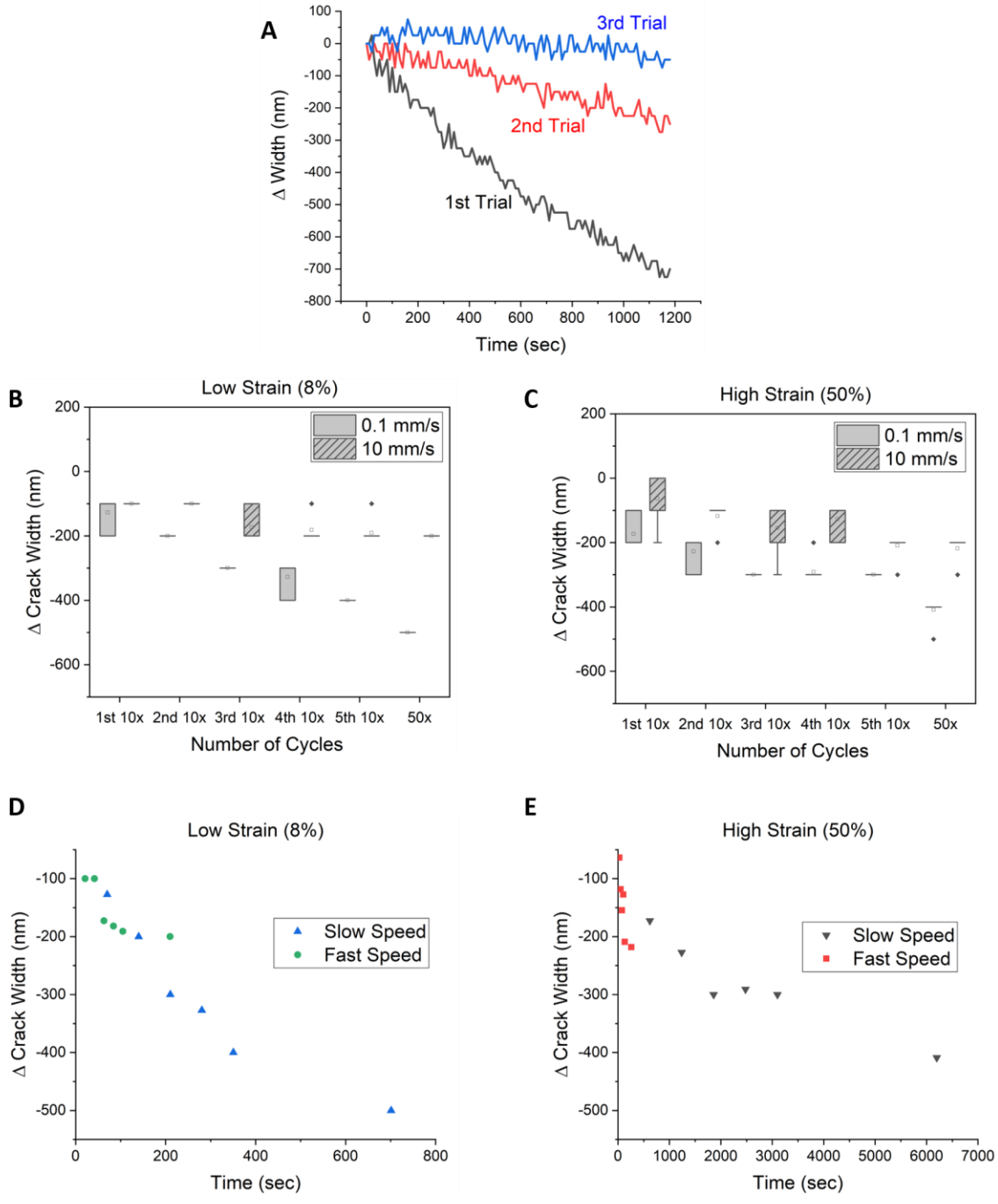

Figure 3.4 Plots of changes in widths with applied strains. (A) The slipping of load from the grips are tracked by changes in widths over time. A PDMS block is stretched to 64% strain and relax after each 20 minutes trial. (B) The effect of slipping at 8% strain on h-

PDMS crack width is cycled through 100 opening and closing cycles at two different speeds. (C) h-PDMS crack width changes at 50% strain. (D) Changes of h-PDMS crack widths over time at 8% strain. (D) Changes of h-PDMS crack widths over time at 50% strain. Slow speed = 0.1 mm/s, fast speed = 10 mm/s.

Table 3.1 Summary of drift over time for low strain and high strain over three 20 minutes tensile cycle trials.

	Δwidth [nm]		
Applied Strain	1	2	3
64.1%	-700	-250	-50
6.40%	-350	-83.3	-33.3

Slippage of the test sample during axial tensile strain also effects the width of the crack channels, i.e. as slippage occurs, the crack channel width decreases. This has relevance here since it is desired to use the crack channels as valves to repeatably stop or allow liquid flow for the delivery of some set volume of liquid. Therefore, the next set of experiments measured the change in the crack width after cyclic opening and closing the crack. The cracks of the hPDMS/PDMS device were opened by applying a strain of 8% or 50% and then closed by returning to a strain of 0%. This opening and closing was repeated and on the 10^{th} cycle, the crack width in the open state was measured optically. This process was repeated for a total of 50 open/close cycles where the crack width was measured every 10 cycles. The results of these experiments are graphed in Figure 3.4B using a low strain of 8% with actuator speeds of 0.1 mm/s and 10 mm/s and then again in Figure 3.4C with a high strain of 50% with actuator speeds of 0.1 mm/s and 10 mm/s. On average, the total changes in widths after 50 cycles was 200 nm for the high strain case (initial crack width

= 6 μm) and 170 nm for the low strain (initial crack width = 1.5 μm) case at 10 mm/s, and then 380 nm for the high strain case and 450 nm for low strain case at 0.1 mm/s. These measurements of Δ crack width are very small and is near the optical limit of the 64x total magnification used. While overall these Δ crack widths are small, these experiments show that there is less change in the nanocrack/nanochannel width after the higher speed cycling for both low and high strain. This behavior is similar to the earlier slippage and spatial accuracy experiments, which showed that in general, faster actuator speeds provides better device performance. From the development process of the stretcher machine and conducting these experiments, it is believed that these small amounts of slippage are due to the hPDMS/PDMS devices slipping minutely in the stretcher mechanism grips. It is difficult to eliminate the grip slippage since tightening of the grips can lead to tearing and failure of the hPDMS/PDMS test sample at the edges of the grip. But even with this amount of slippage present, these experiments and characterization allow for it to be compensated by tensile cycles and choosing appropriate motor speeds.

3.4.3 Femtoliter valve performance characterization

The objective of the development of the on-microscope stretching device and the channel device was to create valves for controlled volume delivery of liquids. The previous sections of this article characterized the stretcher to provide an understanding of the overall system behaviors toward this goal. To investigate the use of the tunable channels as valves, the flow rate through the channels with various channel widths was tested. Tensile strains were applied to the hPDMS/PDMS device to create two crack width cases. The first case created a channel with a 1 μm width and a second case with a crack width of 2.5 μm. In both cases, the fluidic device was loaded with fluorescent sulforhodamine dye or 500 nm

TetraSpeck microspheres in the top horizontal channel and DI water in the bottom horizontal channel. These top and bottom horizontal channels are connected to each other by the vertical crack channels. Figure 3.5A&B show the horizontal top channel loaded with fluorescent dye with the vertical channels closed and thus resulting in the bottom horizontal channel without fluorescent dye. A tensile strain was then applied to the device, causing the vertical channels to open and allow flow of the fluorescent dye from the top horizontal channel to the bottom horizontal channel. Using a pressure of 40 mbar in the top horizontal channel and 20 mbar in the bottom horizontal channel provided by the Elveflow pump, the flow velocity through the 2.5 μm wide channel was 406 μm/s a 1490 μm/s through the 1 μm wide channel. These flow velocities correspond to controllable femtoscale flow rates of 280 fL/sec and 2607 fL/sec for cracks with a depth of 0.7 μm and widths of 1 μm and 2.5 μm respectively. As expected, for a constant pressure gradient across the vertical channel, the flow rate increases with increasing channel width.

This control of the flow was also repeatable as illustrated by Figure 3.5C&D. In these graphs, the vertical cracks were repeatedly open and close by the application of strain on the h-PDMS/PDMS device while a pressure of 40 mbar was applied to the top channel and 20 mbar on the bottom channel. During the cyclic opening and closing, the fluorescent intensity of the bottom channel was measured over time (Figure 3.5C&D). It should be noted that when the vertical cracks are closed, the constant 20 mbar pressure applied to the bottom horizontal channel flushes out all the fluorescent dye and replenishes it with fluorophore-free distilled water. Therefore, the intensity of the fluorescent dye in the bottom horizontal channel corresponds to the volume of liquid delivered through the vertical channesl. The opening and closing of the vertical channels were performed for 100

cycles for the narrow and wide channel width cases. Both cases showed consistent and repeatable fluorescent intensities, i.e. volume delivery. Also, as expected, the volume delivered was dependent on the width of the vertical crack, with the wide crack delivering a greater volume than the narrow crack for a given time (Figure 3.5E).

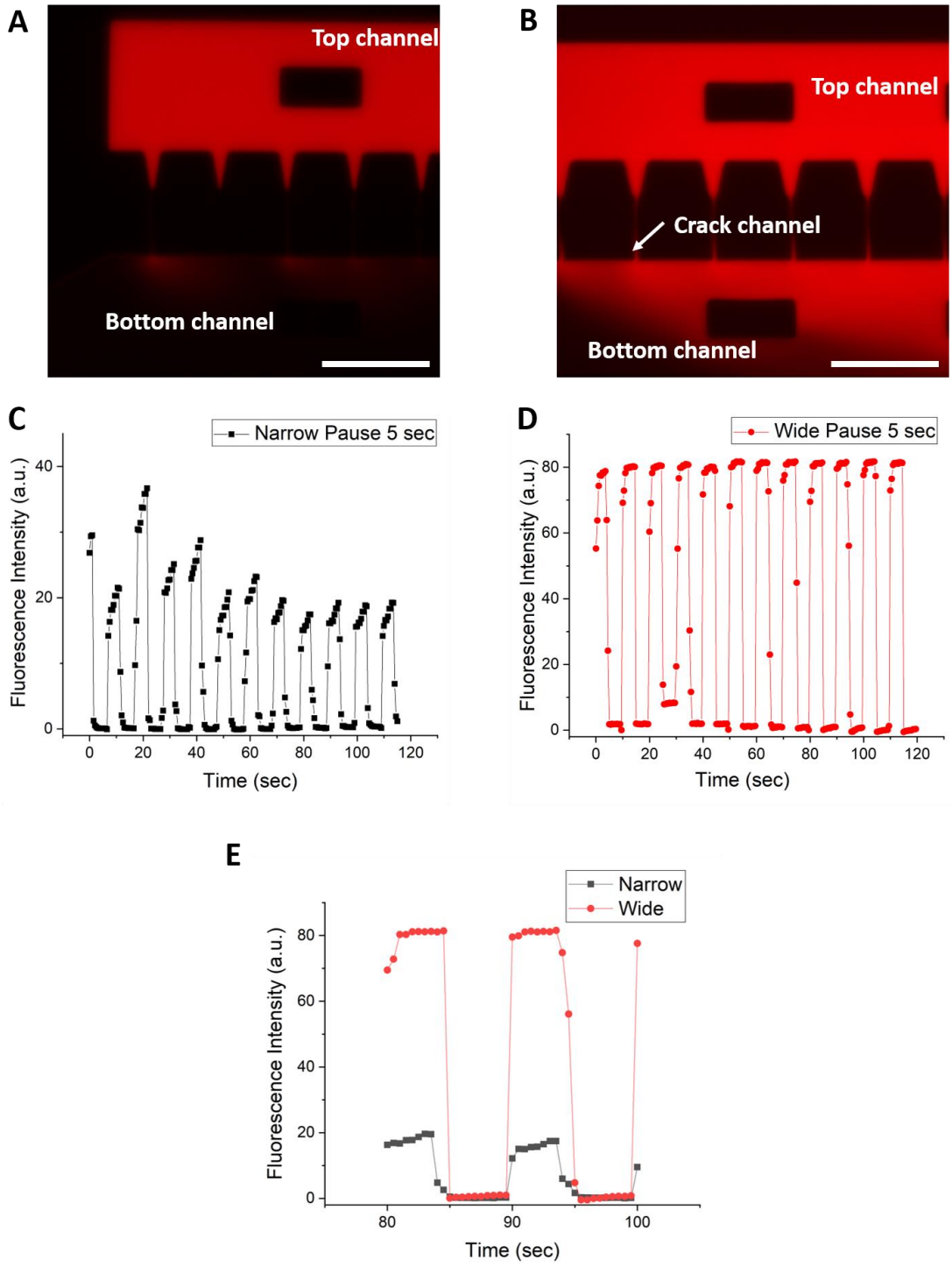

Figure 3.5 Crack channels as femtoliter valves. (A) Fluorescence plume exiting crack channels. (B) Fluorescence intensity reaches maximum in bottom channel. (C) Narrow crack 1 μm channels cycle over time. (D) Wide crack channel 2.5 μm cycling through opening and closing operations. (E) Concentration differences between wide channel and narrow channels. Scale bar = 50 μm.

In order to further understand the volume delivery of the femtoliter valves, the fluorescent intensity at varying distances from the vertical channel's outlet was measured over time (Figure 3.6). The duration of these experiments was 5 seconds, which corresponds to the crack open time of the previous cyclic open/close experiments. Figure 5 illustrates that locations closer to vertical channel's outlet reach saturation of the fluorescence intensity faster. Additionally, the effect of the pressure supplied to the top horizontal channel and the bottom horizontal channel was investigated in these experiments (Figure 3.6). The shortest time to saturation is achieved with the 40 mbar top channel and 10 mbar bottom channel pressure scenario. This was due to the 40/10 pressure scenario creating the largest pressure gradient while also utilizing the lowest horizontal bottom channel pressure. The bottom channel pressure contributes to the pressure gradient across the valved vertical channel, but it also defines the "wash-away" of the fluorophores in bottom channel. Higher bottom channel pressures can cause faster fluorophore wash-away and therefore increase the time to fluorescent saturation and decrease the saturation intensity. This is illustrated by the 40/20 mbar and 30/10 mbar scenarios has the same pressure gradient, but the resulting fluorescence intensity profiles are noticeably different. The greater bottom pressure of the 40/20 scenario increases the wash-away rate and dominates fluoresce intensity behavior. Therefore, the key parameters to control the level of fluorescent saturation and time to reach saturation are the pressure gradient across the valved channel and also the pressure in the bottom channel.

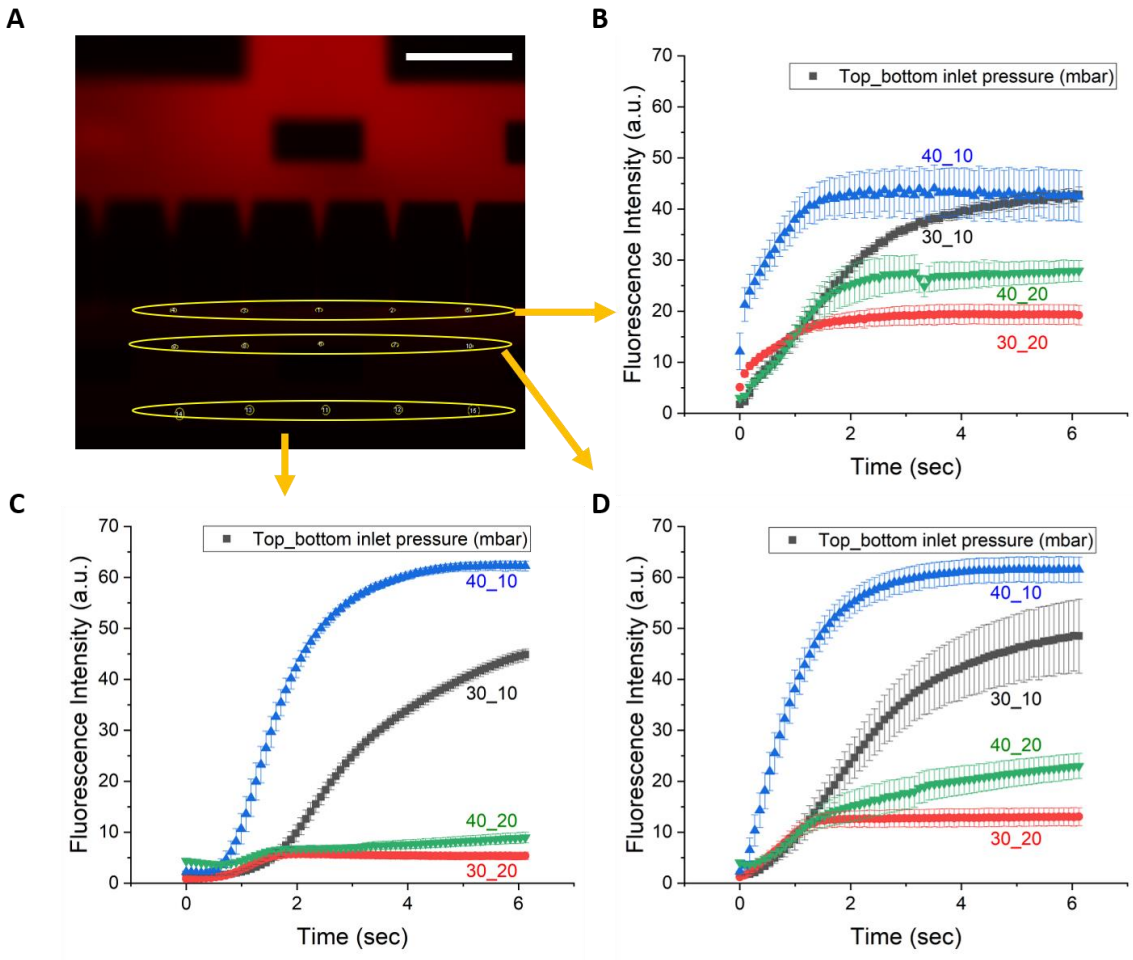

Figure 3.6 Fluorescent intensity at varying distances from the vertical channel's outlet was measured over time. (A) Indicating the location chosen for analysis. (B) Directly adjacent to channel exits, reaching intensity plateau faster. (C) Furthest away from the channel exits, slowest to reach plateau. (D) Slightly removed from exits.

3.5 Conclusion

As we have illustrated in this study, utilizing the precise control of the automated stretcher, we are able to create femtoliter valves for potential applications such as drug release studies. The computer-controlled system allowed us to facilitate cyclic release to target molecules over at least 100 cycles, possessing high durability. The nature of the

tunable channels also implied that the system can be released from the stretcher and be placed in incubation systems for temperature and carbon dioxide level control without the fear of leaky valves releasing target chemicals overtime for long term culture. Our fabrication technique for soft material valving system is a simple and inexpensive alternative that does not require complicated nano-fabrication methods and circumvented the alignment issue faced with most actuator driven membrane deformation technique. We believe that this system would provide solutions to integrated micro/nanofluidic system that requires tight control over fluidic volumes. Furthermore, there are potential applications not explored in this study, such as investigation in mechanical biomarkers in the shape of cell deformation (Hou et al., 2009; Mao and Huang, 2012) through the use of our automated stretcher and crack channels, or the cyclic stress induced mechano-responses from various dimensions or organisms and cells (Gordon and Wang, 2019; Persat, 2017).

3.6 References

Chen, X., and Zhang, L. (2018). Review in manufacturing methods of nanochannels of bio-nanofluidic chips. Sensors Actuators B Chem. *254*, 648–659.

Douglas B. Weibel, Maarten Kruithof, Scott Potenta, Samuel K. Sia, Andrew Lee, and, and Whitesides*, G.M. (2005). Torque-Actuated Valves for Microfluidics.

Godin, J., Chen, C.-H., Cho, S.H., Qiao, W., Tsai, F., and Lo, Y.-H. (2008). Microfluidics and photonics for Bio-System-on-a-Chip: A review of advancements in technology towards a microfluidic flow cytometry chip. J. Biophotonics *1*, 355–376.

Gordon, V.D., and Wang, L. (2019). Bacterial mechanosensing:The force will be with you, always. J. Cell Sci. *132*.

Hamedi, M.M., Ainla, A., Güder, F., Christodouleas, D.C., Fernández-Abedul, M.T., and Whitesides, G.M. (2016). Integrating Electronics and Microfluidics on Paper. Adv. Mater. *28*, 5054–5063.

Hou, H.W., Li, Q.S., Lee, G.Y.H., Kumar, A.P., Ong, C.N., and Lim, C.T. (2009). Deformability study of breast cancer cells using microfluidics. Biomed. Microdevices *11*, 557–564.

Kazoe, Y., Pihosh, Y., Takahashi, H., Ohyama, T., Sano, H., Morikawa, K., Mawatari, K., and Kitamori, T. (2019). Femtoliter nanofluidic valve utilizing glass deformation. Lab Chip *19*, 1686–1694.

Kim, B.C., Moraes, C., Huang, J., Matsuoka, T., Thouless, M.D., and Takayama, S. (2014). Fracture-based fabrication of normally closed, adjustable, and fully reversible microscale fluidic channels. Small *10*, 4020–4029.

Lin, L., Chen, Q., and Sun, J. (2018). Micro/nanofluidics-enabled single-cell biochemical analysis. TrAC Trends Anal. Chem. *99*, 66–74.

Mao, X., and Huang, T.J. (2012). Exploiting mechanical biomarkers in microfluidics. Lab Chip *12*, 4006.

Mawatari, K., Kubota, S., Xu, Y., Priest, C., Sedev, R., Ralston, J., and Kitamori, T. (2012). Femtoliter Droplet Handling in Nanofluidic Channels: A Laplace Nanovalve. Anal. Chem. *84*, 10812–10816.

Napoli, M., Eijkel, J.C.T., and Pennathur, S. (2010). Nanofluidic technology for biomolecule applications: a critical review. Lab Chip *10*, 957.

Persat, A. (2017). Bacterial mechanotransduction. Curr. Opin. Microbiol. *36*, 1–6.

Selvaganapathy, P., Carlen, E.., and Mastrangelo, C.. (2003). Electrothermally actuated inline microfluidic valve. Sensors Actuators A Phys. *104*, 275–282.

Strohm, E.M., Gnyawali, V., Sebastian, J.A., Ngunjiri, R., Moore, M.J., Tsai, S.S.H., and Kolios, M.C. (2019). Sizing biological cells using a microfluidic acoustic flow cytometer. Sci. Rep. *9*, 4775.

Studer, V., Hang, G., Pandolfi, A., Ortiz, M., French Anderson, W., and Quake, S.R. (2004). Scaling properties of a low-actuation pressure microfluidic valve. J. Appl. Phys. *95*, 393–398.

Thorsen, T., Maerkl, S.J., and Quake, S.R. (2002). Microfluidic large-scale integration. Science (80-.). *298*, 580–584.

Unger, M.A., Chou, H.P., Thorsen, T., Scherer, A., and Quake, S.R. (2000). Monolithic microfabricated valves and pumps by multilayer soft lithography. Science *288*, 113–116.

Yang, Y.-W. (2011). Towards biocompatible nanovalves based on mesoporous silica nanoparticles. Medchemcomm *2*, 1033.

CHAPTER 4. SUPER-RESOLUTION IMAGING OF CHROMATIN IN TUNABLE PDMS BASED NANOCHANNELS FOR HISTONE TRANSMISSION

4.1 Abstract

The key to understanding how epigenetics, the study of biological inheritance outside of DNA sequences, affects phenotype is to understand how modifications of epigenetic marks are transmitted. Linearization of chromatin is a strategy to unravel some of the inheritance mechanisms. Tunable channels in the nanoscale resulting from crack formations are presented here for the imaging of linearized chromatin fibers via self-avoidance effect. Generations of periodical nano-crack patterns are achieved by subjecting oxidized polydimethylsiloxane (PDMS) or a nanoscale thin hard PDMS (h-PDMS) system to an applied tensile strain. The cracks can be used as widths adjustable nanochannels capable of completely collapsing channel dimension and immobilizing a single fiber by releasing the applied strain. The device's capability to confine and stretch chromatin fibers are demonstrated with 21.1% of the sample extended to above 80% linearization. *Tetrahymena* is chosen as a model system and strategically tagged and labeled its newly synthesized histone proteins H3. The extracted chromatin is linearized and imaged with super-resolution microscopy showing support for the dispersive model for histone transmission.

4.2 Introduction

Epigenetics is the study of inheritance focusing on mechanisms outside of the nucleotide sequences. A variety of posttranslational modifications, such as histone modifications and DNA methylation are considered to possess epigenetic information (Bird, 2007). It is currently accepted that chromatin structure is important for accessing genetic information, thereby controlling gene transcriptional activity and that histone modifications can control such chromatin structure (Alabert and Groth, 2012; Jenuwein and Allis, 2001; Wolffe and Guschin, 2000). Such epigenetic regulation can be inherited and presents interesting engineering challenges to design systems that are capable of studying chromatin remodeling (Clapier and Cairns, 2009).

Nucleosomes are the basic repeating unit of eukaryotic chromatin, with DNA wrapped around the protein core. Packaging of DNA into large, condensed nucleosomes rely on four histone proteins: H2A, H2B, H3, and H4 (Kornberg, 1974; Parmar et al., 2019). In a cell cycle, chromatin is unwrapped, new histones are synthesized to generate new nucleosomes, and the genetic information carried by histone proteins are distributed onto the DNA. While DNA replication is well understood, details of the mechanism of how such epigenetic information is passed on is less so. One of the biological debates concerns the question of whether histone transmission during DNA replication is of a dispersive or conservative nature (Annunziato, 2012; Saxton and Rine, 2019). Traditionally, studies support the conservative segregation transmission model which suggests that old histones are distributed preferentially onto one arm of the replication fork (Seale, 1976; Weintraub, 1976), with bias towards the leading strand of the replication fork (Seidman et al., 1979). However, disruption of synthesis of *de novo* nucleosomes, may play a role in contributing to conservative results. Conversely, the dispersive segregation model argues for random

distribution to both strands (Cusick et al., 1984; Jackson, 1988; Krude and Knippers, 1991). Also, it is hypothesized, but not clearly shown, that information for gene activity control is carried within chromatin as various DNA-protein structures, and that the heterogeneity of such DNA packaging results in inactive or active transcriptional state. Through the use of strategic histone labeling combined with chromatin fiber linearization and direct imaging analysis with super-resolution microscopy, we may discover new insights on this debate of histone inheritance.

Chromatin immunoprecipitation (ChIP) is the most established histone analysis method (Lippman et al., 2003). ChIP technology has become more powerful and made great strides since its infancy in the form of combining other technique such as DNA sequencing and also microfluidics to improve throughput, automation and reducing sample quantity (Adli and Bernstein, 2011; Wu et al., 2009). However, limitation still exists such as the ability to perform multiple histone modification detections, single molecule analysis or the ability to perform analysis on proteins not directly on top of the DNA backbone (Wardle and Tan, 2015).

Chromatin linearization provides an alternative to ChIP by imaging epigenetic marks along the fibers. Such capability will be helpful in elucidating mechanisms of histone inheritance during DNA replication and is not limited to the protein-DNA analysis but can be expanded into protein-protein analysis. The conventional approach for biopolymer linearization is direct cell shearing with *in situ* hybridization. This method had been adapted successfully for chromatin extension in the study of histone inheritance (Wooten et al., 2018; Xie et al., 2017). Combing is a technique commercially available for stretching arrays of DNA uniformly by meniscus retraction and also found success in stretching

reconstituted chromatin. Despite the high throughput-ness of this technique, biopolymer stretching is determined by the retraction length which is determined by the evaporation rate, therefore limiting the sample range (Cerf et al., 2012). End-tethering technique where conjugated beads are used to captured chromatin and DNA. Assisted by optical or magnetic tweezers, this linearization method is used to investigate the mechanical properties and structure of chromatin (Bennink et al., 2001; Cui and Bustamante, 2000; Kaczmarczyk et al., 2018). However, the external set up necessary to implement this technique poses limitations on adapting it for super-resolution microscopy or electron microscopy.

Another alternative method less pursued is the use of nanochannels to linearize chromatin fibers (Streng et al., 2009; Yeh and Szeto, 2017). This method utilizes entropic traps of the nanochannel, the self-avoidance interactions, polymers will stretch out when confined in spaces below its persistence length. In principle, the nanoconfinement method has the advantage of isolating a single biopolymer, therefore it is possible to study the heterogeneity across multiple fibers, in contrast to techniques requiring pool of samples such as ChIP. Nanoconfinement technique has a long tradition in DNA mapping (Reisner et al., 2012), but has yet to be popularized in chromatin stretching. This confinement method traditionally also presented challenges when adapting to super-resolution microscopy due to movements of molecules interfering with the stochastic imaging capturing methods employed with super-resolution microscopy.

With the use of fractured based PDMS nanochannels, however, we can achieve a high degree of control over nanochannel location and channel cross-sectional size. The chromatin fiber is unscrolled along the channel and the tunable nanochannel can immobilize chromatin by eliminating the physical dimensions of channels, providing

opportunities for epigenomic analysis with super-resolution microscopy. The oxygen permeability nature of PDMS, advantageous for microfluidic cell cultures (Leclerc et al., 2003; Shiku et al., 2006), is however undesirable to the imaging acquisition method in direct stochastic optical reconstruction microscopy (dSTORM) system which requires oxygen scavengers to remove oxygen in solution to prevent photobleaching (van de Linde et al., 2013). In this study, the dye selection to match PDMS system is also investigated, presenting a complete system where chromatin can be effectively linearized and imaged.

4.3 Materials and methods

4.3.1 Oxidized PDMS

Bulk PDMS (Sylgard 184) at 5:1 ratio was cast onto an SU-8 mold and the system is cured overnight in a 65°C oven. The resulting PDMS slabs are oxidized with an oxygen plasma bonder (COVANCE; Femto Science Inc.) at 200 W air plasma for 8 minutes. The oxidized PDMS slab is loaded onto a stretcher, and cracks are formed in the perpendicular direction to the applied strain, Figure 4.1. The pre-cracked oxidized PDMS is then bonded to a thin PDMS membrane (~ 40 μm) after air plasma exposure at 100 W for 30 seconds. The PDMS was also degassed in the oxygen plasma chamber followed by nitrogen venting to limit the amount of oxygen stored in the PDMS prior to use.

4.3.2 h-PDMS

Diluted h-PDMS was prepared with 1.7 g of (7.0-8.0% vinylmethylsiloxane) – dimethylsiloxane copolymer, trimethylsiloxy terminated (VDT-731; Gelest Inc.), 9 μL of platinum-divinyltetramethyldisiloxane complex (SIP6831.2, Gelest Inc.) as catalyst, and

12 μL of 2,4,6,8-tetramethyl-tetravinylcyclotetrasiloxane as moderator (396281 Sigma-Aldrich) followed by two-step dilutions with n-hexane (H303-1; Fisher) to between 1.4% to 1.8%. Slow speed spin coating of the diluted solution was used to achieve a thickness of 200 nm. Bulk PDMS at 5:1 ratio was cast on top of the h-PDMS thin film to create the two-layer system. The h-PDMS cracks are fabricated using the same strategy of stretcher induced cracking followed by plasma bonding to a thin PDMS membrane (~ 40 μm) under air plasma exposure at 100 W for 30 seconds, Figure 4.1.

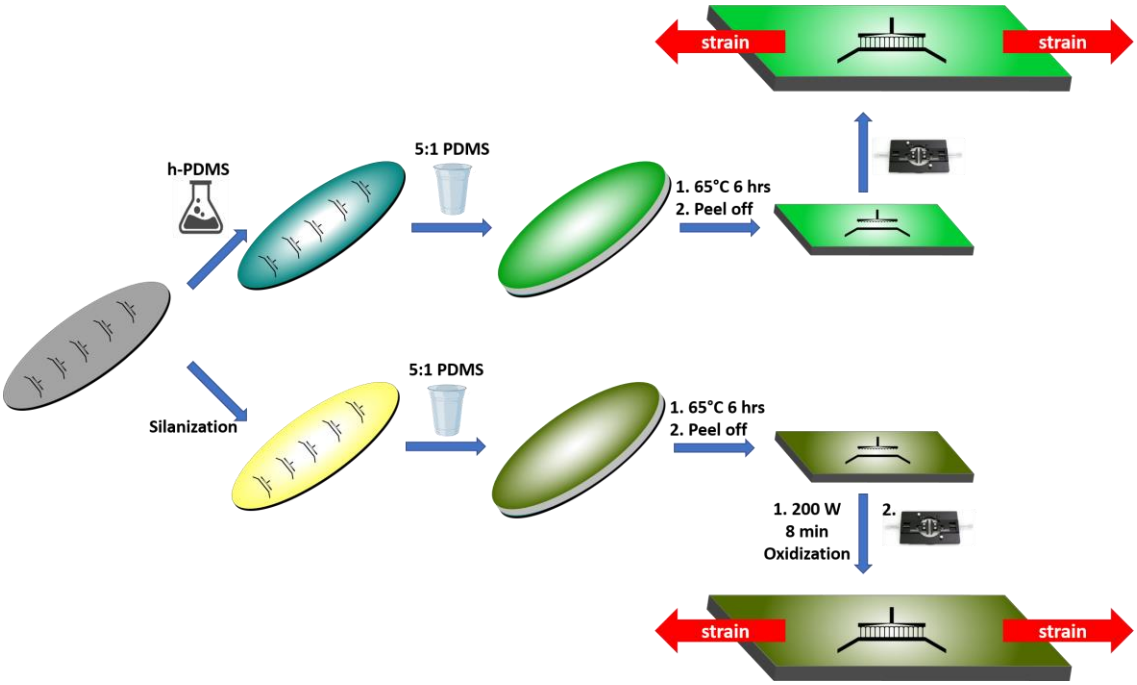

Figure 4.1 Tunable nanochannel fabrications. Top: h-PDMS thin film. Bottom: oxidized PDMS.

4.3.3 Super resolution dye and imaging buffers

d-STORM imaging buffer solution was prepared by mixing 20 µL of 1 M Cysteamine (30070; Sigma), 10 µL of 2-Mercaptoethanol (63689; Sigma), 20 µL of 50x Gloxy mixture and 950 µL of 50 mM Tris-HCl pH 8.0, 10 mM NaCl, 10% (w/v) glucose buffer. The gloxy mixture comprises of 8440 AU glucose oxidase (G2133; Sigma) and 70200 AU Catalase (C40; Sigma) in 1 mL of 50 mM Tris pH 8.0 and 10 mM NaCl buffer (Alonas et al., 2014). The OxEA solution was prepared using a modified protocol from Nahidiazar et all, 50 mM Cysteamine, 3% (v/v) OxyFlour™ (Oxyrase Inc.), 20% (v/v) of sodium DL-lactate solution (L1375; Sigma) in PBS, pH 8.2 (Nahidiazar et al., 2016).

Popular super-resolution dyes Alexa 647 (ThermoFisher), and CF 568 (Biotium) were chosen as model super-res fluorophores. SaraFluor 650B (A202-01; Goryo Chemical), SaraFluor 488B (A218-01; Goryo Chemical), FLIP 565 (FL565; Abberior) and CAGE 635 (CA565; Abberior) were chosen as self-blinking dyes. Alexa 647 and CF 567 were imaged with imaging buffer or OxEA solution, while the self-blinking dyes were imaged with Millipore water.

4.3.4 Tetrahymena model system

A *Tetrahymena* strain, MTT3 HHT1 CHA-CHX, that had been modified with Cd^{2+} induced hemagluttanin (HA) tagged H3 expression was selected as the model system. The culture was grown overnight to its logarithmic phase until ~ $1x10^5$ cell/mL in SPP media. The SPP media is prepared by mixing 10 g protease peptone (211684; VWR), 2 g dextrose (G7528; Sigma), 1 g yeast extract (BP1422; Fisher), 0.03 g ethylenediaminetetraacetic acid

ferric sodium salt (E6760; Sigma) in 1 L of Millipore water (Gorovsky, 1973; Sweet and Allis, 2006).

4.3.5 Chromatin extraction

The MTT3 modified strain was incubated with thymidine analogue BrdU at 10 μM to label its newly synthesized strand for 1 and 2.5 hours. One hour prior to extraction, $CdCl_2$ was added to the Tetrahymena culture to a final concentration of 1 μg/mL. Nuclear isolation procedure was adapted from the octanol-skin method developed by Gorovsky et al. In brief, *Tetrahymena* in the logarithmic phase was spun down and resuspended with 200 mL of medium A, which constituted of 0.1 M sucrose (84097; Sigma), 5 mM magnesium chloride (M1028; Sigma), 4% gum Arabic (G9752; Sigma), 10 mM Tris, pH 7.5 and 10 mM butyric acid (B103500; Sigma) in Millipore water and adjusted the pH to 6.75. The cells are sheared mechanically with a blender along with 1.25 mL 1-ocatanol (8209310100; Sigma), 2 mL of 100 mM phenylmethanesulfonyl fluoride (P7626; Sigma) acting as protease inhibitor, and 2 mL of 0.5 M EDTA (BMA51201; Fisher) to minimize DNA degradation through DNase. The nuclei are collected at 2000 xg for 10 min and resuspended in wash buffer composed of 50mM Tris pH 7.5 and 2mM $MgCl_2$. This is followed by further centrifugation at 3000 xg for 8 min to collect the nuclei and resuspended with nucleoli extraction buffer. The nuclei membrane is then removed via mechanical shearing with a Dounce homogenizer with a tight fitting pestle in the presence of nucleoli extraction buffer 10 mM Tris pH 7.5, 10% glycerol, 0.05 M NaCl, 0.5 mM $MgCl_2$, 1 mM b-mercaptoethanol, 1% Nonidet P-40 and 2 mM PMSF. The nucleoli extract is spun down at 500 xg for 10 min and treated with RNase A for 1 hour at 37°C, Figure 4.2.

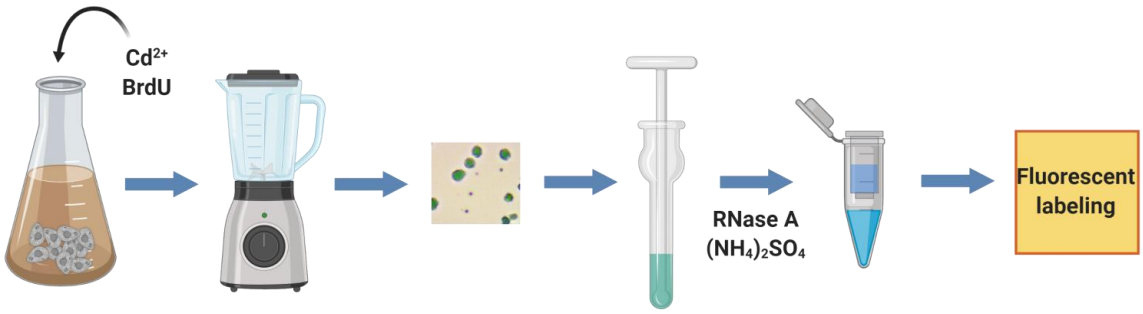

Figure 4.2 Chromatin extraction procedure. After Tetrahymena are grown to its logarithmic phase, BrdU is introduced to the culture for DNA labeling for one cell cycle, while cadmium is allowed to activate HA expression for 1 hour. The cells undergo mechanical lysis with a blender, followed by methyl green verification of nuclei extraction. The nucleoli are extracted with a Dounce homogenizer the resulting solution is treated with RNase and $(NH_4)_2SO_4$ to remove RNA and solubilize non-histone proteins. The extract then undergoes multiple wash step for ion exchange and fluorescent labeling to target HA and BrdU.

4.3.6 Chromatin labeling

Prior to fluorescent labeling, the chromatin extract is treated with ammonium sulfate to solubilize non-histone proteins (Wingfield, 2001), followed by buffer exchange facilitated with centrifugal filter unit to remove undesirable constituents in the nucleoli extraction buffer. The newly synthesized strand of DNA is tagged with anti-BrdU antibody (B8434; Sigma) and the HA-tagged histone H3 is marked by anti-HA antibody (3724S; Cellsignaling) as primary antibodies. After 1 hour incubation at room temperature, the excess antibodies are removed with centrifugal filter units. Secondary antibodies labeled with SaraFluor 650B and FLIP 565 are used to tag anti-BrdU and anti-HA antibodies respectively. Another filter and wash to remove excess secondary antibodies before the

DNA strands are dyed with YOYO-1. A final filter and wash are necessary to remove excess antibodies and dye molecules. The labeled chromatin can be stored at -20 °C.

4.3.7 Chromatin stretching and dye loading

Chromatin are loaded into the h-PDMS nanochannel via the top inlet port. In practice, chromatin solution is diluted with Millipore water at a minimum of 1:100 ratio, and the diluted solution is mixed with 10% Triton X-100 for a final concentration of 1% Triton to facilitate easier loading in small channels. 5 μL of the diluted chromatin solution is loaded onto the top inlet port, and 3 μL of Millipore water is loaded into the left inlet port of the bottom microchannel. The h-PDMS device is mounted onto an automated stretcher, and stretched to ~50 to 70% strain till the crack channels are visible under bright field microscopy. The crack channels are then closed. This action will allow wetting of the crack channels. Further stretching to induce channel opening state will see chromatin fibers enter the crack channels. All motor actions are performed at a fixed 1 mm/s actuator speed in this study. At the stretched state, the h-PDMS nanochannel will open and allow chromatin to flow into the nanochannel through capillary flow. In small conduits with channel diameters falling below the persistence length, local thermodynamics are such that nanoconfinement restricts the conformational degrees of freedom, favoring the stretched conformation that reduces bending energy. Once the strain is released from the stretcher, the channel closes and the trapped chromatin is immobilized, allowing imaging with super-resolution microscopy, Figure 4.3.

The dye solutions are similarly loaded into the oxidized PDMS nanochannel while an external strain is applied via the stretcher to induce channel opening. However, unlike

the h-PDMS nanochannels, oxidized nanochannels often form pockets containing liquid bubbles when the channels are closed (Matsuoka et al., 2012). These trapped dye solutions often occurred when channel collapsing occurred too fast, and also from incomplete through cracks, cracks that did not propagate from the top microchannel all the way through to the bottom microchannel, therefore forming trapped solutions. Both the oxidized device containing fluorophore bubbles and the h-PDMS device with the trapped chromatin were imaged by a Bruker Vutara 352 direct stochastic optical reconstruction microscopy (dSTORM). The devices are placed on top of a No. 0 glass coverslip to prevent devicd bending.

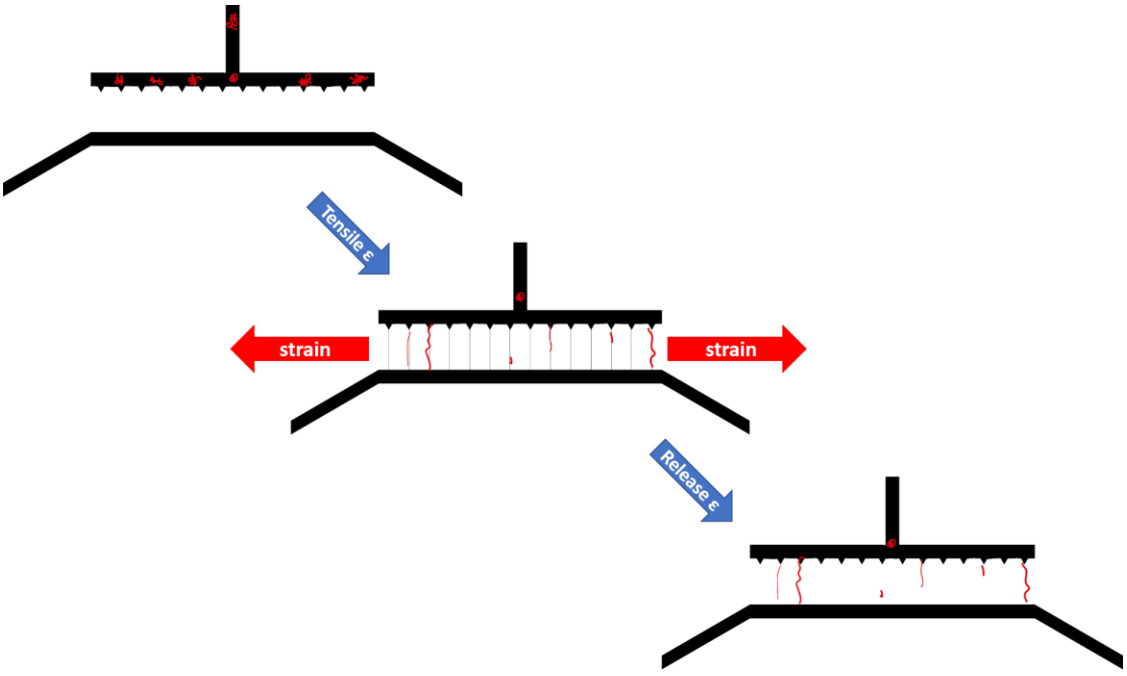

Figure 4.3 Schematic representation of chromatin loading into nanochannels. Channels are closed at initial loading of chromatin solution, as tensile strain increases, the nanocracks open and chromatin unravel from its densely packed state into linearized fibers. Releasing the applied tensile strain return the PDMS to its relaxed state, closing the nanochannels and immobilizing the chromatin.

4.4 Results and discussions

4.4.1 Dye selection

The d-STORM microscope system is capable of achieving a maximum resolution 20 nm which is ideal for protein analysis. However, the oxygen permeability of PDMS rendered the photoactivable fluorophores that d-STORM relied on ineffective. Matching an appropriate fluorophore and buffer system is therefore crucial in PDMS based devices. By trapping the fluorophores in the fluid pockets of oxidized PDMS, we're able to recreate similar environment experienced by immobilized chromatin in nanocracks. Fluid pockets are first verified with standard fluorescent microscope (DMi8; Leica) before transferring to the d-STORM system. As expected, imaging Alexa 647 and CF 568 in conventional Gluox based imaging buffer is inoperable, Figure 4.4 (A)&(B). The reducing agents were not able to overcome the oxygen rich environment and cannot revert the fluorophores back into its dark triplet state, therefore the fluorophores bleached out under less than a hundred frames of acquisitions.

Using oxygen scavenging solution such as OxEA, we hope to remove oxygen released by PDMS. We are able to observe photo-blinking, as shown in Figure 4.4(C)&(D). However, compared to an ideal situation where Alexa and CF dyes are exposed to copious amount of imaging buffer or OxEA solution, photo-bleaching is still significant. Approximately five hundred frames were collected to reconstruct back into Figure 4.4(C)&(D) before the dyes could no longer switch between its dark and fluorescent states. This is a much lower number of acquisition frames compared to the thousands of frames typical of super-resolution imaging procedures. It is therefore suspected that the amount of

oxygen removed is insufficient via the OxEA method. Another cause for the sub-optimal effectiveness is due to the small dimensions of nanochannels, especially when the tunable channels are closed where only minute quantity of fluorophores are exposed to the imaging or OxEA buffer, consequently insufficient quenching.

With the use of self-blinking dyes SaraFluor 650B, SaraFluor 488B, FLIP 565 and CAGE 635, however, we're able to overcome the oxygen-rich, low buffer volume environment of a PDMS nanochannel, Figure 4.4 (E)-(G). These are all rhodamine based fluorophores, while the SaraFluor family utilized the intramolecular spirocyclization to convert between triplet and ground states spontaneously (Uno et al., 2014, 2018), FLIP required activation with UV light for activation (Roubinet et al., 2018), and the CAGE dye is released by photoactivation (Fölling et al., 2007). These fluorophores were initially synthesized with the intent to overcome the UV damages or the harsh environment of imaging buffer associated with super-resolution imaging, but also are suitable for our nanochannels.

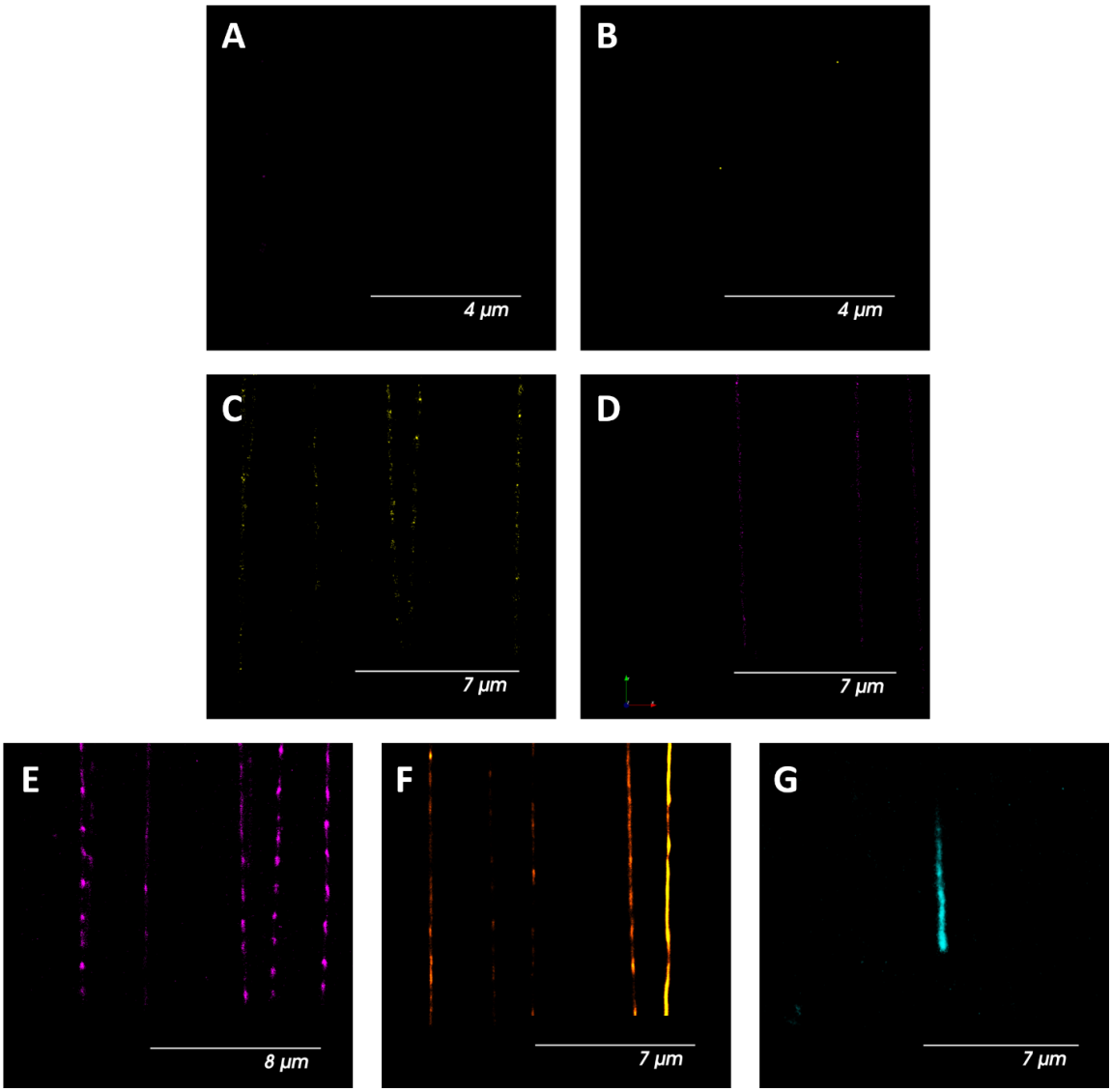

Figure 4.4 Super-resolution imaging dye and buffer selection. (A) Alexa 647 in thiol containing imaging buffer. (B) CF 568 in thiol containing imaging buffer. (C) Alexa 647 in OxEA buffer. (D) CF 568 in OxEA buffer. (E) SaraFlour 650B in water. (F) FLIP 565 in water. (G) SaraFlour 488B

4.4.2 Chromatin super-resolution microscopy

A key factor in choosing the tunable nanochannels over the standard nanochannel technique for chromatin elongation is in its compatibility with super-resolution

microscopy. Figure 4.5 demonstrated how a trapped chromatin in an open nanochannel conduit is still wriggling around. Significant movement is observed within just 10s of seconds, therefore rendering it impossible to use the localized fluorophores for image reconstruction, as d-STORM requires thousands of acquisitions, consequently minutes of imaging time. It is also worth noting that the chromatin molecule is not linearized as well as in the completely closed channel. Figure 4.6 illustrated the problems of image reconstruction with an opened channel in a d-STORM system.

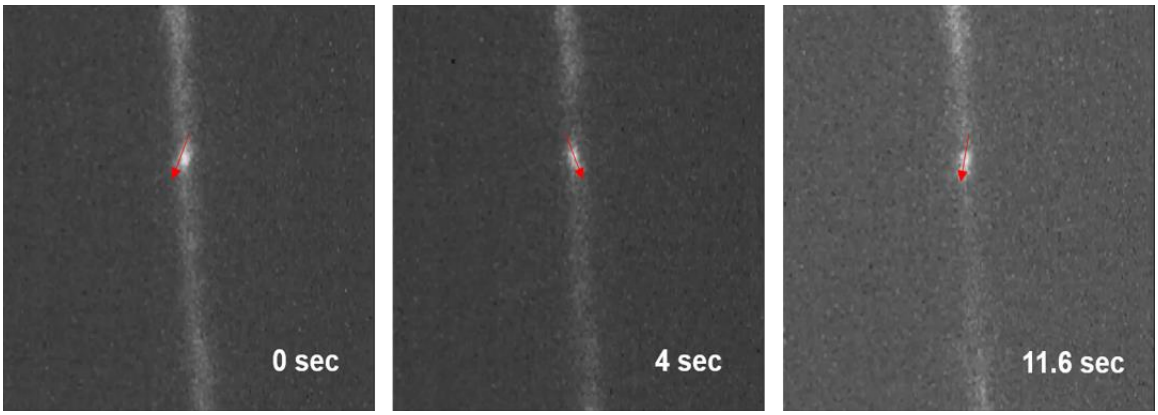

Figure 4.5 Wide field image of a chromatin fiber in an opened nanochannel. The video was captured with a wide field camera. The chromatin is unstretched and moving in the open channel.

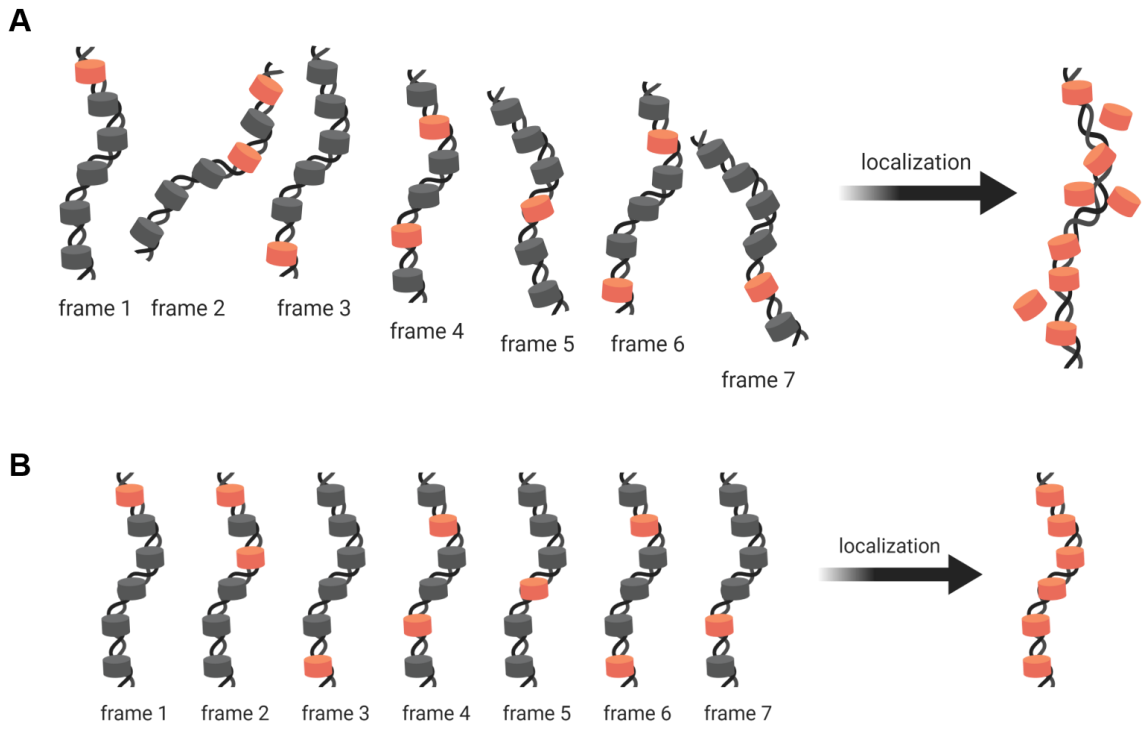

Figure 4.6 Schematic demonstration of the importance of localization in super-resolution microscopy. (A) Wriggling movements of a chromatin in opened channel and moving downstream by residual fluidic flow. (B) Immobilization of a chromatin fiber in tunable channel allowing successful fluorescence localization.

4.4.3 Chromatin elongation with nanochannels

The 1.4-1.8% h-PDMS thin film layer was spin coated to approximately 200-300 nm in thickness to limit the z-dimension of the nanocracks, while the widths of the nanochannel is controlled by an external tensile strain. The pre-patterned features guided the generation of the hundreds of parallel cracks, allowing for high throughput analysis. A horizontal strain is applied to open the nanochannels and allow chromatin fibers to enter the narrow conduits. The system is optimized for easy loading of the densely packed chromatin molecules by capillary and hydrodynamic flow without the use of outside forces

such as an electric field. Multiple parallel nanochannels also increases the chances of chromatin fibers being captured per h-PDMS device. This compensates for the low chromatin concentration used in the experiment to ensure only one copy of chromatin fiber is trapped per channel. Due to nanoconfinement, the chromatin will elongate, and with the unique tunable feature of our stretch assisted system, we're able to completely close the channel, further confining and immobilizing the chromatin.

The rDNA mini-chromosome extracted from the macronuclei of *Tetrahymena* is a palindromic dimer at 21 kb in size. Assuming 0.3 nm per DNA base pair and the beads-on-a-string model in which the DNA wrapped around the histone octamer every 1.65 turns (Luger et al., 2012; Schlick et al., 2012), we estimated that the completely linearized Tetrahymena mini-chromosome is ~ 4 μm in length at full extension. The extensions of 38 captured chromatin are tabulated in Table 4.1. Approximately 21.1% of the chromatin fibers are above 80% linearized. However, nearly half of the chromatin remained in its globular form. This is possibly due to nucleosome-nucleosome interactions or other electrostatic interactions between proteins and DNA.

Table 4.1 Chromatin extension and number of chromatin categorized as following dispersive histone transmission model. a/b with a denoting the number of dispersive, and b the total number of chromatin at its corresponding extension regime.

Chromatin Extension	% Chromatin	# Dispersive
<40%	44.7%	15/17
40-60%	18.4%	6/7
60-80%	7.9%	2/3
80-100%	21.1%	6/8
100-110%	7.9	3/3

4.4.4 Histone inheritance

Tetrahymena nucleosomes are constituted of one tetramer $(H3/H4)_2$, and two (H2A/H2B) dimers. Due to the transcription-dependent turnover behavior of the H2A/H2B dimers, much of the focus on histone segregation is centered on the (H3/H4) tetramer. Nucleosome assembly is linked to both replication-coupled and replication-independent mechanisms (Robinson and Schultz, 2003; Yang et al., 2016). It is therefore imperative to choose a model system whose histone deposition has been well-characterized. *Tetrahymena* presents such a model. Its histone deposition is strictly replication coupled for canonical H3 but replication-independent for the H3.3 variant, while deposition of H4 can be both replication-coupled and replication-independent in Tetrahymena (Belotserkovskaya et al., 2003; Cui and Bustamante, 2000; Cui et al., 2006; Liu et al., 2004). Furthermore, non-nucelosomal H3 level is low and actively turned over. It is therefore possible to identify the newly synthesized histone vs old, existing histones prior to treatment, with cadmium induced expression of HA tagged H3 for replication-dependent histone deposition pattern. Dose test is performed to ensure sufficient HA expression without cell death from Cd^{2+} over-exposure. The cadmium treatment is also limited to 1 hour, less than a full cell cycle thereby limiting the number of newly synthesized HA-tagged histone. Successful rDNA extraction is verified via electrophoresis.

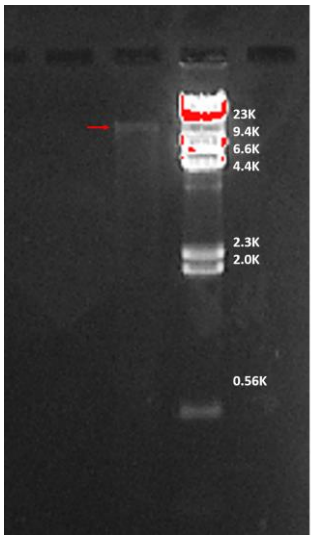

Figure 4.7 Gel electrophoresis of extracted Tetrahymena rDNA. The assessment is performed in TAE buffer at 100 V and the DNA ladder are from λ-DNA/HindIII Marker (FERSM0101; FisherSci).

Anti-HA antibodies and anti-BrdU antibodies labeled the newly synthesized histone and newly synthesized DNA strand respectively. BrdU is a thymidine analog that has a small bias towards the leading strand over the lagging strand (Loidl and Scherthan, 2004; Yu et al., 2018). Figure 4.8(F) contrasts the visualization capabilities between conventional optical microscopy vs a super-resolution microscopy such as dSTORM. It also demonstrates how the tunable nanochannels are capable of immobilization of biopolymers, allowing confinement and reconstruction of fluorophores signals. Figure 4.8(C)&(D) explained the predicted image type for the two models of histone segregation. Nucleosome distribution spacing is reported to be 199 bp which would correspond to 20 nm, therefore we expect that any spacing larger than 20 nm between histone signals following the predicted pattern in the top panel would fall into the dispersive segregation model. Only chromatin that exhibited greater than 60% of extension was used for

categorizing conservative or dispersive distribution. A total of 11 out of 14 linearized chromatin fibers were classified as potentially dispersive. Using a two-tailed z-score population test. There is significant difference at $p < 0.05$ ($p = 0.00252$) between the two groups.

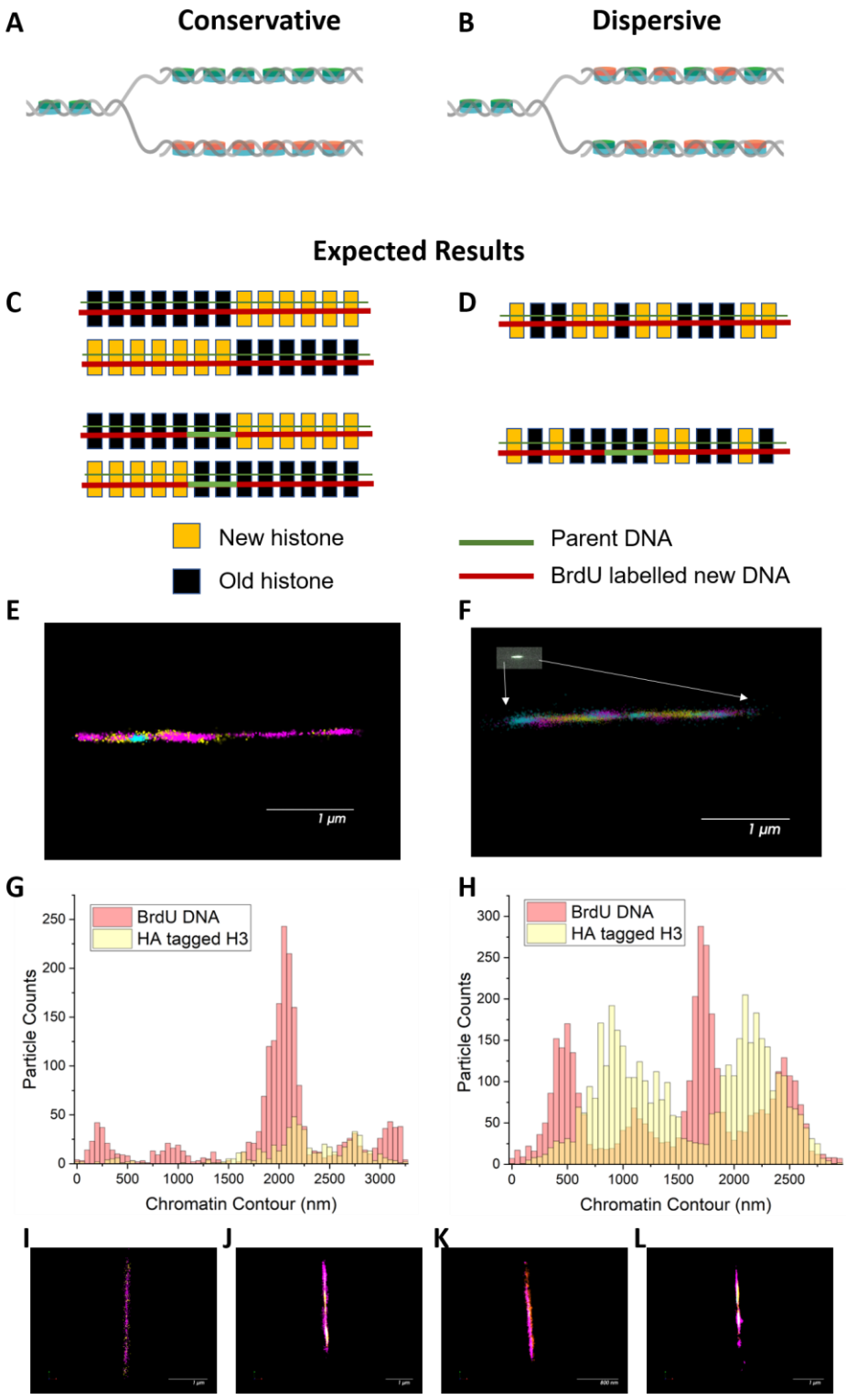

Figure 4.8 Histone inheritance models, predicted results and super-resolution images. (A) Conservative model. (B) Dispersive model. (C) Predicted results of conservative model in our labeling system. (D) Predicted result of dispersive model. (E) Super-resolution

results showing a chromatin fiber categorized as conservative distributions. (F) Super-resolution results showing a chromatin fiber categorized as dispersive distributions for statistical analysis tabulated in Table 4.1. The wide field image of the same strand is show on top left hand corner. (G) Overlapping histogram showing binned particle counts of the chromatin fiber in E. (H) Overlapping histogram of the chromatin fiber in F. (I) - (L) Additional supporting super-res images of dispersive chromatin fiber categorized as dispersive distributions. YOYO-1 (cyan), BrdU (pink), H3 (yellow) for (E), (F), (I) - (J).

4.5 Conclusion

The consensus is that epigenetics may be important in our understanding of a multitude of disease such as Alzheimer, cancer and even the increase of diseases state with age (Feinberg, 2007). At present, limitation shared by current chromatin analysis technique is the inability to be adapted to clinical settings, where epigenetic biomarkers may be useful in diagnosing potential diseases (Berdasco and Esteller, 2019). However, plenty of questions remain to be answered in our understanding of epigenome before it can be translated into clinical practice, and there is no “one size fits all” technique available for studying epigenetics. The method presented above aimed to take advantage of the direct imaging capability in linearized DNA/chromatin to investigate histone inheritance. The combination of nanochannel with super-resolution technique, however, presented two primary challenges: 1) movements of molecules within channels, and 2) oxygen rich environment of PDMS. The two were resolved by combining size-adjustable tunable nanochannels, where chromatin loading was optimized by channel widening with tensile strain and channel collapsing to immobilize chromatin, and the use of self-blinking dye to circumvent insufficient quenching of fluorophores. Chromatin extracted from

Tetrahymena were linearized in this platform for histone inheritance analysis, and found that dispersive segregation of newly synthesized histone H3 is preferred.

4.6 References

Adli, M., and Bernstein, B.E. (2011). Whole-genome chromatin profiling from limited numbers of cells using nano-ChIP-seq. Nat. Protoc. *6*, 1656–1668.

Alabert, C., and Groth, A. (2012). Chromatin replication and epigenome maintenance. Nat. Rev. Mol. Cell Biol. *13*, 153–167.

Alonas, E., Lifland, A.W., Gudheti, M., Vanover, D., Jung, J., Zurla, C., Kirschman, J., Fiore, V.F., Douglas, A., Barker, T.H., et al. (2014). Combining Single RNA Sensitive Probes with Subdiffraction-Limited and Live-Cell Imaging Enables the Characterization of Virus Dynamics in Cells. ACS Nano *8*, 302–315.

Annunziato, A.T. (2012). Assembling chromatin: The long and winding road. Biochim. Biophys. Acta - Gene Regul. Mech. *1819*, 196–210.

Belotserkovskaya, R., Oh, S., Bondarenko, V.A., Orphanides, G., Studitsky, V.M., and Reinberg, D. (2003). FACT Facilitates Transcription-Dependent Nucleosome Alteration. Science (80-.). *301*, 1090–1093.

Bennink, M.L., Leuba, S.H., Leno, G.H., Zlatanova, J., de Grooth, B.G., and Greve, J. (2001). Unfolding individual nucleosomes by stretching single chromatin fibers with optical tweezers. Nat. Struct. Biol. *8*, 606–610.

Berdasco, M., and Esteller, M. (2019). Clinical epigenetics: seizing opportunities for translation. Nat. Rev. Genet. *20*, 109–127.

Bird, A. (2007). Perceptions of epigenetics. Nature *447*, 396–398.

Cerf, A., Tian, H.C., and Craighead, H.G. (2012). Ordered Arrays of Native Chromatin Molecules for High-Resolution Imaging and Analysis.

Clapier, C.R., and Cairns, B.R. (2009). The Biology of Chromatin Remodeling Complexes. Annu. Rev. Biochem. *78*, 273–304.

Cui, Y., and Bustamante, C. (2000). Pulling a single chromatin fiber reveals the forces that maintain its higher-order structure. Proc. Natl. Acad. Sci. U. S. A. *97*, 127–132.

Cui, B., Liu, Y., and Gorovsky, M. a (2006). Deposition and function of histone H3 variants in Tetrahymena thermophila. Mol. Cell. Biol. *26*, 7719–7730.

Cusick, M.E., DePamphilis, M.L., and Wassarman, P.M. (1984). Dispersive segregation of

nucleosomes during replication of simian virus 40 chromosomes. J. Mol. Biol. *178*, 249–271.

Feinberg, A.P. (2007). Phenotypic plasticity and the epigenetics of human disease. Nature *447*, 433–440.

Fölling, J., Belov, V., Kunetsky, R., Medda, R., Schönle, A., Egner, A., Eggeling, C., Bossi, M., and Hell, S.W. (2007). Photochromic Rhodamines Provide Nanoscopy with Optical Sectioning. Angew. Chemie Int. Ed. *46*, 6266–6270.

Gorovsky, M.A. (1973). Macro- and Micronuclei of Tetrahymena pyriformis: A Model System for Studying the Structure and Function of Eukaryotic Nuclei. J. Protozool. *20*, 19–25.

Jackson, V. (1988). Deposition of newly synthesized histones: hybrid nucleosomes are not tandemly arranged on daughter DNA strands. Biochemistry *27*, 2109–2120.

Jenuwein, T., and Allis, C.D. (2001). Translating the Histone Code. Science (80-.). *293*, 1074–1080.

Kaczmarczyk, A., Brouwer, T.B., Pham, C., Dekker, N.H., and van Noort, J. (2018). Probing Chromatin Structure with Magnetic Tweezers. (Humana Press, New York, NY), pp. 297–323.

Kornberg, R.D. (1974). Chromatin structure: A repeating unit of histones and DNA. Science (80-.). *184*, 868–871.

Krude, T., and Knippers, R. (1991). Transfer of nucleosomes from parental to replicated chromatin. Mol. Cell. Biol. *11*, 6257.

Leclerc, E., Sakai, Y., and Fujii, T. (2003). Cell Culture in 3-Dimensional Microfluidic Structure of PDMS (polydimethylsiloxane). Biomed. Microdevices *5*, 109–114.

Lippman, Z., May, B., Yordan, C., Singer, T., and Martienssen, R. (2003). Distinct Mechanisms Determine Transposon Inheritance and Methylation via Small Interfering RNA and Histone Modification. PLoS Biol. *1*, e67.

Liu, Y., Mochizuki, K., and Gorovsky, M.A. (2004). Histone H3 lysine 9 methylation is required for DNA elimination in developing macronuclei in *Tetrahymena*. Proc. Natl. Acad. Sci. U. S. A. *101*, 1679–1684.

Loidl, J., and Scherthan, H. (2004). Organization and pairing of meiotic chromosomes in the ciliate Tetrahymena thermophila. J. Cell Sci. *117*, 5791–5801.

Luger, K., Dechassa, M.L., and Tremethick, D.J. (2012). New insights into nucleosome and chromatin structure: an ordered state or a disordered affair? Nat. Rev. Mol. Cell Biol. *13*, 436–447.

Matsuoka, T., Kim, B.C., Huang, J., Douville, N.J., Thouless, M.D., and Takayama, S. (2012). Nanoscale squeezing in elastomeric nanochannels for single chromatin linearization. Nano Lett. *12*, 6480–6484.

Nahidiazar, L., Agronskaia, A. V., Broertjes, J., van den Broek, B., and Jalink, K. (2016). Optimizing Imaging Conditions for Demanding Multi-Color Super Resolution Localization Microscopy. PLoS One *11*, e0158884.

Parmar, J.J., Woringer, M., and Zimmer, C. (2019). How the Genome Folds: The Biophysics of Four-Dimensional Chromatin Organization. Annu. Rev. Biophys. *48*, 231–253.

Reisner, W., Pedersen, J.N., and Austin, R.H. (2012). DNA confinement in nanochannels: physics and biological applications. Reports Prog. Phys. *75*, 106601.

Robinson, K.M., and Schultz, M.C. (2003). Replication-independent assembly of nucleosome arrays in a novel yeast chromatin reconstitution system involves antisilencing factor Asf1p and chromodomain protein Chd1p. Mol. Cell. Biol. *23*, 7937–7946.

Roubinet, B., Bischoff, M., Nizamov, S., Yan, S., Geisler, C., Stoldt, S., Mitronova, G.Y., Belov, V.N., Bossi, M.L., and Hell, S.W. (2018). Photoactivatable Rhodamine Spiroamides and Diazoketones Decorated with “Universal Hydrophilizer” or Hydroxyl Groups. J. Org. Chem. *83*, 6466–6476.

Saxton, D.S., and Rine, J. (2019). Epigenetic Memory Independent of Symmetric Histone Inheritance. BioRxiv 760801.

Schlick, T., Hayes, J., and Grigoryev, S. (2012). Toward convergence of experimental studies and theoretical modeling of the chromatin fiber. J. Biol. Chem. *287*, 5183–5191.

Seale, R.L. (1976). Studies on the mode of segregation of histone nu bodies during replication in HeLa cells. Cell *9*, 423–429.

Seidman, M.M., Levine, A.J., and Weintraub, H. (1979). The asymmetric segregation of parental nucleosomes during chrosome replication. Cell *18*, 439–449.

Shiku, H., Saito, T., Wu, C.-C., Yasukawa, T., Yokoo, M., Abe, H., Matsue, T., and Yamada, H. (2006). Oxygen Permeability of Surface-modified Poly(dimethylsiloxane) Characterized by Scanning Electrochemical Microscopy. Chem. Lett. *35*, 234–235.

Streng, D.E., Lim, S.F., Pan, J., Karpusenka, A., and Riehn, R. (2009). Stretching chromatin through confinement. Lab Chip *9*, 2772.

Sweet, M.T., and Allis, C.D. (2006). Transformation of Tetrahymena thermophila by Electroporation. CSH Protoc. *2006*, pdb.prot4502.

Uno, S., Kamiya, M., Yoshihara, T., Sugawara, K., Okabe, K., Tarhan, M.C., Fujita, H., Funatsu, T., Okada, Y., Tobita, S., et al. (2014). A spontaneously blinking fluorophore

based on intramolecular spirocyclization for live-cell super-resolution imaging. Nat. Chem. *6*, 681–689.

Uno, S., Kamiya, M., Morozumi, A., and Urano, Y. (2018). A green-light-emitting, spontaneously blinking fluorophore based on intramolecular spirocyclization for dual-colour super-resolution imaging. Chem. Commun. *54*, 102–105.

van de Linde, S., Aufmkolk, S., Franke, C., Holm, T., Klein, T., Löschberger, A., Proppert, S., Wolter, S., and Sauer, M. (2013). Investigating Cellular Structures at the Nanoscale with Organic Fluorophores. Chem. Biol. *20*, 8–18.

Wardle, F.C., and Tan, H. (2015). A ChIP on the shoulder? Chromatin immunoprecipitation and validation strategies for ChIP antibodies. F1000Research *4*, 235.

Weintraub, H. (1976). Cooperative alignment of nu bodies during chromosome replication in the presence of cycloheximide. Cell *9*, 419–422.

Wingfield, P. (2001). Protein precipitation using ammonium sulfate. Curr. Protoc. Protein Sci. *Appendix 3*, Appendix 3F.

Wolffe, A.P., and Guschin, D. (2000). Review: Chromatin Structural Features and Targets That Regulate Transcription. J. Struct. Biol. *129*, 102–122.

Wooten, M., Nizami, Z., Yang, X., Snedeker, J., Ranjan, R., Kim, J.M., Urban, E., Tran, V., Buss, J., Gall, J., et al. (2018). Asymmetric histone incorporation during DNA replication in Drosophila male germline stem cells. SSRN Electron. J.

Wu, A.R., Hiatt, J.B., Lu, R., Attema, J.L., Lobo, N.A., Weissman, I.L., Clarke, M.F., and Quake, S.R. (2009). Automated microfluidic chromatin immunoprecipitation from 2,000 cells. Lab Chip *9*, 1365.

Xie, J., Wooten, M., Tran, V., and Chen, X. (2017). Breaking Symmetry − Asymmetric Histone Inheritance in Stem Cells. Trends Cell Biol. *27*, 527–540.

Yang, J., Zhang, X., Feng, J., Leng, H., Li, S., Xiao, J., Liu, S., Xu, Z., Xu, J., Li, D., et al. (2016). The Histone Chaperone FACT Contributes to DNA Replication-Coupled Nucleosome Assembly. Cell Rep. *14*, 1128–1141.

Yeh, J.-W., and Szeto, K. (2017). Electrophoretic stretching and imaging of single native chromatin fibers in nanoslits. Biomicrofluidics *11*, 044108.

Yu, C., Gan, H., Serra-Cardona, A., Zhang, L., Gan, S., Sharma, S., Johansson, E., Chabes, A., Xu, R.M., and Zhang, Z. (2018). A mechanism for preventing asymmetric histone segregation onto replicating DNA strands. Science (80-.). *361*, 1386–1389.

CHAPTER 5. CONCLUSIONS AND FUTURE OUTLOOK

5.1 Conclusion

It has become more apparent over the last decade that interdisciplinary studies are needed to tackle complex biological questions. With the advent and commercialization of super-resolution microscopy, imaging nanoscale markers on biological materials had become an accessible research technique, by passing the relatively stringent sample preparation requirement in tradition nanoscale analysis such as AFM, SEM or TEM. Whereas in the field of fabrication, soft materials have emerged as an alternative for micro-, nano- patterning for relatively inexpensive platform. Combined with automation and computer vision imaging processing capabilities, the landscape of biological research had opened up opportunities to address unresolved questions. This dissertation took advantage of the above techniques and adapted them to create a system capable of chromatin linearization for nanoscopy protein imaging.

Three key targets were met in this project: (1) the development of reproducible tunable nanochannel arrays for nanofluidics; (2) the design of customized automated stretcher capable of sustaining high load for fracturing super thin film; and (3) the analysis of histone segregation during replication from linearized chromatin fibers with super-resolution microscopy.

Chapter 2 looked at the fabrication of nanochannels with h-PDMS. Expanding upon previous works and our understanding of the multi-layered fracture system, nanochannels are generated at the tip of v-notches that served as both strain relieving and stress focusing

points. Furthermore, the morphology and of the cracks can be tuned by using different photoresists. The automated stretcher presented in Chapter 3 was used not only to generate nano- and micro- cracks, but also to control the precise crack widths. The precision and accuracy of the motor motion is analyzed with and without load. Combing this stretcher with the tunable cracks, the opening and closing of the nanochannel is used as femtoliter valves. Finally, in Chapter 4, we applied the system to biological application. The ability of the h-PDMS nanochannels to linearize biopolymers were verified with both DNA and chromatin. In this study, histone proteins are labeled and extracted from *Tetrahymena*, followed by linearization in nanochannel. Releasing tensile strain collapsed the nanochannels effectively immobilizing chromatin to overcome the wriggling motion of a molecule inside a channel due to residual hydrodynamic flow. Fluorophore and imaging solution were paired with stochastic optical reconstruction microscopy for. The results provide evidence supporting dispersive distribution of histone inheritance.

5.2 Additional comments

In chapter 2, I pointed out that at the percentage of dilution we're dealing with, using high spin speeds (>1000 rpm) would result in blotchy spin-coated film. This is true in the case of low volume/mass of diluted h-PDMS. When depositing chemicals onto the silicon substrate, for typical high speed spin coating, it is usually unnecessary to cover the surface of the substrate completely, a quarter size is usually recommended, but this would result in the blotchy distribution described in chapter 2. However, when a larger amount of diluted h-PDMS is used, e.g 2.7 mL in conjunction with high speed spin coating, blotchy surface can be avoided. The profilometer result showed that the 1% h-PDMS thin film was still wavy, Figure 5.1, at 3000 rpm using a 4 μm SU-8 2 mold, but potentially more uniform

than the low spin speed version presented in Chapter 2. An alternative strategy for avoiding waviness of the film would be to use a different solvent.

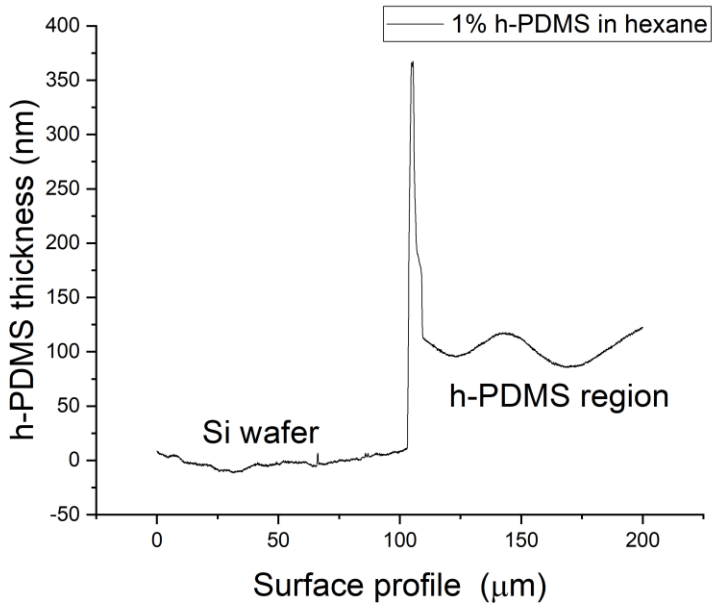

Figure 5.1 Distribution of a 3000 rpm spin coated 1% h-PDMS film.

The data was collected using a contact profilometer with stylus radius 2.5 μm, at a force of 1.00 mg and theoretical resolution of 0.022 μm/sample. The film measurement procedure was the same as described in section 2.3.4. The sharp peak in the figure was a result from 1. a slight curling/folding of the film, and 2. the stylus being caught at the edge of the film.

The effect of the SU-8 species to the high speed spin coated film was not investigated. I would postulate that the repelling contribution resulted from contact angle differences would be lessened, but the differences in different height of SU-8 may

contribute to other variations of distribution results due to the local kinetics and thermodynamic changes. The trend between film thickness and spin coating speed was not investigated systematically either, therefore how different percent dilution would affect the resulting film at different spin speed is unknown.

5.3 Future direction

The immediate short-term goal is to increase sample size of linearized chromatin. We obtained positive results indicating dispersive inheritance, but a larger sample size is needed for more accurate statistical analysis.

As we have demonstrated, the tunable channels can be combined with our automated stretcher system as valving system. This provides a great opportunity for studying femtoliter scale drug releases, with the stretcher, there is potential for kinetic studies by simply opening and closing of the femtoliter valves, and combined with channel confinement, there is the possibility to simultaneously look at mechanoresponsive tests and drug analysis.

For longer term objectives, the system can be further optimized for visualization of proteins. In the practical application perspective, even though this system is capable of chromatin loading by simple capillary and gravity effects, the loading efficiency can be potentially improved upon with the use of an external electric field. Furthermore, by matching polymerization rate with the nanochannel closing rate, the extensions of linearized DNA have been shown to increase by repeated opening and closing of nanochannels. With the automated stretcher where we can precisely control the rate of channel narrowing, it is therefore possible to translate this technique to improve chromatin

linearization outcome. An alternative method is to combine with magnetic setup where we implement the end-tethering magnetic beads technique into our immobilization method.

In principle, nanochannel arrays system provides the possibility to analyze single molecule. This is particular useful in providing heterogeneity information and can be applied to tracking posttranslational modifications with antibody labeling. For example, the loss of tri-methylation on H3K27 has been proposed as a potential biomarker for nerve sheath tumor. Another lysine residue that may be of interest is H3K9 and its role in chromatin assembly. It has been suggested that heterochromatin protein 1 (HP1) is involved in the recruitment of Su(Var)3-9 for H3K9 methylation, therefore by inhibiting HP1 function and targeting H3K9 modification, we may be able to shed light on the mechanism of chromatin assembly.

From a material standpoint, the extreme high strain required for h-PDMS nanochannel generation is not favorable for practical use. Channel widening is even more perilous due to the inlet and outlet ports produced by biopsy punches, for the nanoscale channel, bulk PDMS often experiences catastrophic fracture. The shape of the ports is also greatly deformed, rendering the system unusable with fluidic syringe pump and tubing setup. The search for an alternative elastomeric system is recommended. In terms of the h-PDMS fractured based channel system, I believe that its key strength lies in the lower microscale regime, between 1 μm to 10 μm. The micron size regime crack system does not suffer from the operational inconveniences stated above, and are reliable platforms for microfluidic studies. For instance, sickle cells deform into its sickle shape under low oxygen environment and polymerized with neighboring hemoglobin. The process is not reversible and as the elasticity of the cell is decreased, the tunable channel system could

serve as a research or even be translated into a diagnostic platform. Other potential applications such as cell deformation studies and mechanical biomarkers or inducing mechano-responses through cyclic stress by automated stretcher would be ideal questions to tackle with this platform.